Spectroscopic Studies of Paramagnetic Impurities in Solid Parahydrogen Matrix

YAN, Lei

A Thesis Submitted in Partial Fulfillment
of the Requirements for the Degree of
Doctor of Philosophy
in
Chemistry

The Chinese University of Hong Kong
July 2011

ProQuest LLC.
789 East Eisenhower Parkway
P.O. Box 1346
Ann Arbor, MI 48106 - 1346

Thesis Committee

Prof. Zhifeng Liu (Chair)

Prof. Man-Chor Chan (Thesis Supervisor)

Prof. Bo Zheng (Committee Member)

Prof. Shi-Chung Cheung (External Examiner)

Prof. Shuiming Hu (External Examiner)

Abstract

In this thesis, spectroscopic studies of the catalyzed nuclear spin conversion (NSC) of *ortho*-H_2 molecules in solid H_2 matrix and the high-resolution Fourier transform infrared (FTIR) absorption spectra of O_2 and NO embedded in matrices of *para*-H_2 crystals are presented. For NSC of *ortho*-H_2, the catalyzed conversion rate was found to be diffusion-determined by setting up systematical kinetic studies of solid H_2 samples dopant with O_2 and NO. The factors affecting diffusion process were discussed; For the high-resolution FTIR of O_2 and NO, sharp lines presumable due to rotational structure were observed. Based on the observation, preliminary analysis of the spectrum was discussed for O_2 and NO, respectively.

摘要

在研讀博士學位期間，我們搭建了一套以固態仲氫分子為基質材料的基質隔離高分辨紅外吸收光譜實驗儀器。我們研究了正氫分子在固態下，被氧氣和一氧化氮分子催化的核自旋弛豫現象，以及氧氣和一氧化氮分子在固態仲氫基質中的高分辨紅外光譜。對於前者，我們通過系統的動力學研究，證實了正氫分子的催化核自選弛豫速度與該分子在固體裡的擴散相關，並闡釋了影響正氫分子擴散的因素；而對於後者，由於仲氫分子基質隔離實驗的種種優點，我們得到了催化劑分子，如氧氣和一氧化氮，在基質中的高分辨紅外吸收光譜，並對光譜的震動和轉動結構作出解釋。在這篇論文裡，相關的實驗和理論將得到詳細的闡釋和說明。

Acknowledgements

I would like to express my pure-hearted gratitude to all those who gave me the possibility to complete this thesis, especially my supervisor Prof. M. C. Chan. In the past 4 years study under Prof. Chan's kind guidance, what I have learned are not only the experimental techniques and theoretical knowledge, but also the enthusiasm to the scientific research. He is full of passion and energy, even when he faces blows and obstacles. Moreover, he is a gentle man with many humors and his amiable personality makes him very easy to stay with. I will always remember encourages he gave to me when I encountered the heavy frustration in my study and living in my early days in Hong Kong. It was him who helped me out of the trouble and established my self-confidence. I would say that I cannot accomplish my postgraduate study without his encouragement and help.

I also appreciate so much for the supporting I received from Prof. Shuiming Hu in USTC. He taught me how to operate instruments in his laboratory with great patience, and discussed the results with great enthusiasm. The time I spent there turned out to be very pleasant and fruitful, and the results I obtained there are very important for the completion of this thesis. Thanks are also given to the Mr. Lei Wu working there, who usually helped me out of the trouble during the experiments.

I would also not forget my groupmates for their very kind supporting. I have learned a lot from discussions with Mr. Zhenwu Liao, received many suggestions from Miss. Mei Yang, and obtained many supports from Miss. Yan Song. Their selfless help

contributes my advancement.

Besides that, the staff and fellows from other research groups and technical supporting unit, also gave me a lot of supporting and suggestions which made my research progress much more smooth. Thanks also come to them.

Last but not the least, I cannot forget to mention my family members-my mother, my father and my lovely girlfriend Sissi. Their deep love and care in every possible way cannot be expressed by any word in the world. I will dedicate this thesis to them.

Table of Contents

List of Figures

List of Tables

CHAPTER I. Introduction

Matrix isolation spectroscopy has been developed into a very unique and powerful technique for spectroscopic studies for molecules since the 1930s. The earliest isolation experiments was conducted by Lewis and co-workers,[1] which involved UV-Visable absorptions of species frozen in transparent, low temperature organic glasses. Later in 1950s, George Pimentel, often referred as the "father of matrix isolation", initially used higher-boiling inert gases like xenon and nitrogen as the trapping media for reactive species and performed some important experiments which could be regarded as the prototype of the modern matrix isolation spectroscopy.[2] After that, countless studies on matrix-isolation were carried out in the 1950s and 1960s. These researches included studying atomic species, mainly metal atoms, diatomics (e.g. C_2, CN, LiF, NF, OH, OF, ScO, Si_2, SiO and S_2), triatomics (e.g. Al_2O, BeF_2, $BeCl_2$, C_3, CCO, CCl_2, CNN, KrF_2, S_3 and $XeCl_2$) and tetra-atomic and larger species (e.g. CH_3, CCl_3, S_4, SiF_3 and XeF_4), with Ar, Kr, Xe, N_2, O_2, CH_4, CO, SF_6 and numerous other molecules being the host materials.[3]

In addition to studies concerning small molecules in inorganic chemistry, larger

organic molecules also drew substantial attention. In the 1970s, a number of investigations on the IR spectrum of cyclobutadiene isolated in argon and nitrogen matrices were reported.[4-6] These initial works stimulated the applications of matrix isolation for mechanistic studies in organic chemistry in the next two decades. A detailed review can be found for those interested in this aspect.[7] Nowadays, with the development of commercially available cryostats and specialized spectroscopic techniques, challenging molecular systems with high impact in various disciplines have been studied, such as binuclear metal complexes, highly photolabile carbonyl oxides, and even DNA bases, *etc.*[8]

The success of matrix-isolation spectroscopy can be ascribed to the following reasons. First of all, the low temperature and the rigidity of the matrix minimize the motions of isolated species. In addition, only very few energy levels of the guest molecules are occupied at cryogenic temperature to simplify the spectral pattern in the spectrum, which may facilitate the assignments of the spectroscopic features. Secondly, the inert matrix environment minimizes the reactivity of the isolated species, resulting in prolonged lifetime, which makes it possible to characterize the reaction intermediates. Thirdly, the much higher density in the solid state compared to the gas phase should in principle improve dramatically the detectability of the isolated species. It is the combination of these advantages that makes the matrix isolation studies guide the way for the corresponding gas phase studies, providing new insights into chemical reaction mechanism.

On the other hand, matrix-isolation spectroscopy also displays a number of

limitations. The isolated species is subject to significant intermolecular interactions in the matrices. These interactions, which are anisotropic depending on the crystal structure of the matrix, not only give rise to additional splitting of energy levels to complicate the spectral pattern but also give rise to fast relaxation processes and homogeneous broadening of spectral transitions. Together with the inhomogeneous broadening arising from the various microscopic environment surrounded the isolated species as well as the possible amorphous structure in the solid matrix, serious spectral line broadening may wash out the fine structures of the molecular motions, as compared to the case in the gas phase study. The typical observed spectral width in the solid state is on the order of a few cm^{-1}. In addition, matrix-isolated molecules may have limited degree of freedom for internal motion due to strong intermolecular interactions. It is common that only vibrational transitions can be observed in the spectrum of rare gas matrices.[9] These limitations make the identification of unknown species much more difficult in case the corresponding gaseous data are unavailable.

Solid *para*-H_2, in contrast, had been demonstrated in numerous spectroscopic experiments since the 1980s, a unique matrix material for spectroscopic studies at very high resolution.[10-26] In these experiments, very sharp transitions were observed, allowing the rovibrational structures as well as crystal field splitting due to anisotropic interactions to be resolved. By analyzing the fine structures of the rovibrational spectra, one can obtain a wealth of information on selection rules, intermolecular interactions, as well as relaxation process.

The unprecedented spectroscopic properties of solid *para*-H_2 matrix reflect how

unique this system is. As the simplest molecular solid, solid H_2 distinguishes itself from other conventional matrix materials such as rare gas and nitrogen by properties arising from the combination of light mass, small molecular size, large intermolecular separation, and weak intermolecular interactions.[11] Due to the large separation and weak intermolecular interactions, molecules isolated are only slightly perturbed in solid H_2 compared to the gas phase. The properties can therefore be elucidated from the first principle.

Depending on the relative orientation of spin of the protons forming the molecules, H_2 may exhibit a total nuclear spin of 0 or 1, corresponding to *para*-H_2 and *ortho*-H_2, respectively. In the ground electronic state, *ortho*-H_2 and *para*-H_2 occupy levels with opposite parity that makes the conversion between them forbidden under the Born-Oppenheimer approximation. The light mass of H_2, however, causes breakdown of the Born-Oppenheimer approximation and very slow conversion between *ortho* and *para* species. As a result, H_2 molecules with different total nuclear spin behave as distinct species and thus are called nuclear spin modifications. The relative abundance of these two species in the matrix dramatically affects the appearance of the spectra of isolated molecules. For pure *para*-H_2 matrix at cryogenic temperature, molecular wavefunctions are spherically symmetric and thus anisotropic interactions vanish. However, trace amount of *ortho*-H_2 is unavoidable in *para* enriched matrices. It is this small amount of *ortho*-H_2 that makes solid *para*-H_2 a fascinating system. The weak anisotropic interactions due to *ortho*-H_2 give rise to a multitude of phenomena unique to solid *para*-H_2 that have been extensively studied.

The conversion between *ortho* and *para*-H_2, while usually very slow, can be catalyzed by the presence of paramagnetic molecules, which provide inhomogeneous magnetic fields. In solid H_2 matrix the study of the conversion rate will shed some light on the diffusion between the catalyst molecules and H_2. On the other hand, only very few kinetic studies of *ortho/para* conversion of H_2 have been reported. We therefore set out to systematically study the kinetics of catalytic *ortho/para* conversion of H_2 in the solid state.

During my residence as a Ph.D student, I was involved in constructing an experimental system for high resolution spectroscopy of solid hydrogen. Following the completion of the system, I investigated the kinetics of nuclear spin conversion dynamics of H_2 in the solid state catalyzed by O_2 and NO, respectively. In addition, the high resolution FTIR spectra of these two molecules embedded in solid *para*-H_2 matrix were also obtained for the first time.

In the rest of the thesis, I will first discuss the properties of hydrogen in details in Chapter II. This is followed by the detailed description of experimental apparatus, as well as experimental procedure in Chapter III. The kinetic studies of the nuclear spin conversion of H_2 molecule in the solid will be presented in Chapter IV, followed by the spectroscopic studies of O_2 and NO doped in the solid H_2 matrix in Chapter V.

CHAPTER II. Properties of Hydrogen

Hydrogen molecules, which are considered the simplest and most fundamental molecules of all, are composed of two protons separated by about 0.74 Å and surrounded by two electrons. Over the years, properties of hydrogen have been studied due to their simplicity. Results from these studies have been well documented.[27] Some fundamental physical properties are listed in Table 1.[28] H_2 molecule and its isotopes form the simplest molecular solids due to the combination of the light mass, weak intermolecular interactions, and large intermolecular separation. On the other hand, properties of the solids are dominated by quantum effects, such as quantized molecular rotation and vibration and quantum diffusion of molecules, *etc.* To aid our discussions in the following chapters, some spectroscopic properties of hydrogen molecules and solid hydrogen are discussed below.

Table 1: Tabulated physical properties of hydrogen molecule

Molecular weight	2.0157
Normal boiling point	20.278 K

Density at normal boiling point	0.07087 g/cm^3
Triple point	13.813 K
Pressure at triple point	52.82 Torr
Density at triple point	0.07709 g/cm^3
Critical point	32.976 K
Pressure at critical point	9.6976×10^{3} Torr
Density at critical point	0.03145 g/cm^3
Heat of vaporization	4.459×10^{9} erg/g
Heat of fusion	5.82×10^{8} erg/g
Specific heat	9.67×10^{7} erg/g
Thermal conductivity	11.8×10^{7} erg/cm s K
Viscosity	135.4 micropoise
Surface tension	1.93×10^{3} dyne/cm
Dielectric constant	1.2285
Molar volume of solid at 4.2 K	
99.8% p-H_2	23.064 cm^3/mole
n-H_2	22.820 cm^3/mole

II.1 Nuclear Spin Modifications of Hydrogen Molecules

The coupling of the two spin-1/2 protons of a hydrogen molecule gives rise to two types of H_2 corresponding to different total nuclear spin (I). Orhtohydrogen (*ortho*-H_2) are those with parallel nuclear spin to give I=1 and parahydrogen (*para*-H_2) are those with anti-parallel nuclear spin to give I=0. The Pauli principle requires that,[29] *para*-H_2 molecules populate only the rotational levels with even J quantum number, while *ortho*-H_2 molecules populate only the rotational levels with odd J quantum number. Since the conversion of nuclear spin is strictly forbidden from the parity considerations under the Born-Oppenheimer approximation (adiabatic approximation), only extremely slow nuclear spin conversion occurs due to the breakdown of the approximation. In fact it takes months for *para*-H_2 gas to reach thermal equilibrium mixture at room temperature. As a result, H_2 molecules with different total nuclear spin can be practically treated as different species. They are often referred to nuclear spin modifications. According to the quantum theory of angular momentum,[30] the I=1 molecules have $2I+1=3$ allowed M_I projections while I=0 molecules have only one. Thus, the I=1 species is three times as abundant as the I=0 species at high temperature with M_I called basically degenerate. Traditionally, the more abundant nuclear spin modification is termed *ortho* while the less abundant one *para*. In the case of H_2, *para*-H_2 is species with even J and I=0 and *ortho*-H_2 is the species with odd J and I=1, at a ratio of 1 to 3 at room temperature.

This abundance ratio keeps unchanged even if H_2 molecules are cooled from room temperature to cryogenic temperature, because of the extreme slow conversion rate

between *ortho* and *para* species. Each nuclear spin modification will reach the Boltzmann distribution respectively as the temperature dropping down, i.e. *para*-H_2 populating essentially the $J = 0$ rotational state while *ortho*-H_2 populating essentially the $J = 1$ rotational state to give an *ortho/para* ratio of 3:1 at cryostat temperature. The conversion between *ortho*-H_2 and *para*-H_2 can be catalyzed by paramagnetic materials, which provide a non-uniform magnetic field.[31] In preparing *para*-enriched samples of hydrogen for our experiments, an inline *ortho-para* converter was installed in our gas handling system. The detailed discussion will be presented in Chapter III. The kinetic studies of *ortho-para* conversion of H_2 molecules in the solid state catalyzed by the paramagnetic dopant molecules, O_2 and NO, will be presented in Chapter IV and Chapter V.

II.2 Spectroscopic Properties of Hydrogen Molecules

Pure rotational and rovibrational transitions of H_2 are forbidden due to the lack of permanent or vibration-induce dipole moment. However, transitions via quadrupole mechanism and Raman scattering have been observed[32]. In addition, transitions due to intermolecular multipole-induced-dipole interactions have also been observed in high pressure gas as well as in the condensed phases.[10] The non-spherical charge distribution in H_2 molecules leads the existence of multipole moments, which induce dipole moments on the nearby molecules. In the case of high pressure gas, two interacting H_2 molecules act as a unit to absorb light that leads to a spectral transition. For instance, the quadrupole moment of molecule 1 induces a dipole moment on molecules 2 due to its

isotropic and anisotropic polarizabilities. The induced dipole moment then interacts with the oscillating electric field associated with light to cause a spectral transition on molecule 1 (known as single transition) or on both molecules 1 and 2 (known as double transitions). Single transitions are often due to the isotropic polarizability in which molecule 2 simply serves as an antenna for the absorption of light for molecule 1 even though molecule 2 does have the induced dipole moment. In the case of double transitions, both molecules change quantum states by absorbing one photon. By applying this idea to the solid state and taking into account the point symmetry of crystal environment, Van Kranendonk established a rigorous theory to interpret the rovibrational spectrum of solid hydrogen. Dipole moments induced by mutipole moments of different order are responsible for different infrared transitions according to the selection rules. The lowest three nonzero multipole moments of H_2 are quadrupole (4-pole), hexadecapole (16-pole), and tetrahexacontapole (64-pole), which give rise to $Q(\Delta J = 0)$ and $S(\Delta J = 2)$ branches, $U(\Delta J = 4)$ branch, and $W(\Delta J = 6)$ branch single transitions, respectively. Compare to the usual multipole transitions, the multipole-induced transitions have the same selection rule but much stronger intensity that makes them observable in the solid state. To date, 128 pole-induced transitions with $\Delta J = 8$ has been reported.[8] The long range multipole-multipole interactions split the otherwise degenerate M_J levels corresponding to different orientation of the molecules in the solid state. The narrow linewidth in solid hydrogen allows the splitting to be resolved. This opens a new system for direct probing of the anisotropic intermolecular interactions using high resolution spectroscopy. For more detailed discussion of the

theoretical aspects of rovibrational spectroscopy of solid hydrogen, a number of excellent reviews are available.[10,11,17]

II.3 Properties of Solid Hydrogen

Properties of solid hydrogen have been extensively studied and documented in many aspects for years.[10,11,17] It has been known that H_2 crystals are formed in either hexagonal close-packed or face-centered cubic structures, with the nearest neighbor distance of 3.79 Å. Because of the weak intermolecular interactions and large intermolecular separations, H_2 molecules in crystals retain their identity with properties not too different from those in the gas phase. Interactions in solid *para*-H_2 are mainly isotropic dispersion interactions. Since the $J=0$ rotational wavefunction has a spherical shape, *para*-H_2 molecules in the $J=0$ state have no permanent electric moments of any order. In other words, anisotropic interaction is absent in pure *para*-H_2 crystals. On the other hand, *ortho*-H_2 molecules occupying the $J=1$ rotational quantum number have a small permanent quadrupole moment. As a result, the small *ortho*-H_2 concentration in *para*-enriched H_2 crystals leads to the electric quadrupole-quadrupole (EQQ) interactions, which are the most dominant anisotropic interactions in the crystal.

As mentioned above, properties of solid hydrogen are dominated by quantum effects. Like He, solid hydrogen is considered a translational quantum crystal that is signified by the large compressibility. The exceptional softness of solid H_2 allows its density to be doubled from its zero pressure value by applying a pressure of 20 kbar,

whereas such pressure change only results in a few percent increase in other solids.[28] In addition, solid H_2 exhibits large amplitude of zero-point lattice vibration.[33] The mean amplitude of the zero-point lattice vibration in solid *para*-H_2 amounts to almost 20% of the nearest intermolecular distance. Molecules are therefore not sharply located at the equilibrium lattice sites. Because of these properties, impurity molecules with size much greater than that of H_2 can fit into the lattice sites of solid H_2 without causing much crystal defect.

Solid hydrogen displays unusually high thermal conductivity which may be ascribed to its large zero-point lattice vibration. The thermal conductivity of *para*-enriched solid hydrogen containing 0.2% *ortho*-H_2 is 50 $Wm^{-1}K^{-1}$ at 4.2 K,[10] which is comparable to that of Cu, and is almost one order of magnitude greater than those of rare gas crystals.[34] The high thermal conductivity of solid *para*-H_2 allows fast thermal exchange with the surroundings. This property is particularly important for the annealing process of matrix material. For instance, the fast dissipation of excess energy produced in the photolysis of molecules in solid H_2 is crucial in stabilizing the photofragments in the H_2 crystal.

Molecule in solid H_2 is only slightly perturbed by the solid state environment as shown in numerous experiments. Molecules in solid H_2 are expected to have internal motions, such as rotation and vibration, like in the gas phase. Based on thermodynamic considerations, Pauling predicted the hindered rotation of H_2 in the solid.[35] Rovibrational spectra of solid H_2 were observed in the 1950s. The spectral pattern of the spectra indicates that H_2 molecules have nearly free rotation and vibration. As a result,

both J and ν remain good quantum numbers. The weak anisotropic intermolecular interactions, on the other hand, give rise to the fine structures in the spectra. These interactions are also responsible for many other observed effects such as multipole-induced dipole and relaxation processes.

In forming a *para*-enriched H_2 crystal from the gas state, the spatial distribution of metastable *ortho*-H_2 molecules is expected to be completely random. On the other hand, the EQQ interaction between pairs of *ortho*-H_2 molecules gives lower energy. The thermodynamic equilibrium therefore favors the formation of *ortho*-H_2 pairs. It has been observed that the pair configuration can be achieved by keeping the crystal in a prolonged time.[18] This phenomenon, known as rotational diffusion, has been ascribed to quantum mechanical resonant conversion of an *ortho-para* to *para-ortho* pair by intermolecular magnetic dipole-dipole interaction. A rate constant of about 2 hours^{-1} was predicted using this model, which is consistent with the experimental observations.

II.4 Solid Hydrogen as Matrix Material

One of the most important considerations of matrix isolation spectroscopy is the choice of the matrix material. Factors influencing the choice of dopant/host combination include: spectral compatibility, chemical reactivity, dopant isolation efficiency, and stringency of cryogenic requirements for achieving thermally stable low vapor pressure samples.[36] Common matrix materials such as rare gases and N_2 all share the common characteristics of being chemically inert, and low vapor pressure, free of absorption spectra that would interfere with spectroscopic detection of the isolated species, rigid.

Argon and nitrogen are readily and cheaply available, being obtained in large quantities by fractional distillation of liquid air. The other rare gases are more expensive, being present in the atmosphere only in very small amounts. Over the years, lots of spectroscopic studies of stable and unstable species using these matrix materials can be found in literature.

In most spectroscopic studies using rare gases and N_2 matrices, rotational structures were not resolved due to both homogeneous and inhomogeneous line broadening. The rigidity of these matrix materials also increase the chances of trapping dopant molecules in the interstitial holes instead of lattice sites, resulting in amorphous structure and inhomogeneous broadening. For instance, vibrational transition of CO in Kr and Xe matrices exhibits a typical width of 2 cm^{-1}.[37]

The absence of fine structures in vibrational bands limits our understanding of the detailed interactions and dynamics of molecules in condensed phases. In addition, the rigidity of these conventional matrices may limit the studies of chemical reactions at cryogenic temperatures, as strong interactions from the surrounding matrix molecules may significantly distort reaction potential surfaces from those in the gas phase.[38] As a result, the mobilities of matrix-isolated molecules are significantly reduced to allow diffusion that is necessary for reactions at cryogenic temperature.

Solid H_2 has never been considered as a good matrix material until recently. As discussed above, the softness, low melting point, and high vapor pressure at cryogenic temperature of solid H_2 makes it difficult to prepare a sample of matrix with good optical quality. Nevertheless, high resolution spectroscopic work of solid H_2 in the later 1980s

have demonstrated that optically transparent samples of more than 10 cm long can be prepared by depositing gas on a cold surface at about 7 K.[14] Together with the exceptionally narrow observed linewidth, solid *para*-H_2 has presented its potential as a matrix material for high resolution spectroscopy. The large lattice constant and the large amplitude of zero-point lattice vibration in solid hydrogen provide more free space for guest molecules than other matrices. For instance, the intermolecular distance in solid *para*-H_2 (3.79 Å) is considerably large than the interatomic distance in solid Ne (3.16 Å), as well as other rare gas solids, while the pair potential between H_2 molecules is similar to that between Ne atoms. Moreover, the large lattice constant of solid *para*-H_2 results in weak intermolecular interactions between the dopant molecules and matrix molecules compared with those in rare gas matrices. Together with the large Debye frequency of lattice vibration of solid *para*-H_2, the lifetime of a guest molecule in excited states becomes much longer in *para*-H_2 matrix. This may be qualitatively ascribed to the origin of the sharp spectral linewidth observed in solid *para*-H_2. In some cases, the spectral linewidth is sharp enough to resolve not only J structure but also the M structure due to the orientation of the molecules in the anisotropic crystal field environment.[25] The analysis of such fine structures promises rich information to shed light on understanding intermolecular interactions as well as molecular motion in the condensed phase.

The laser studies of *ortho*-H_2, HD and D2 in *para*-H_2 crystals marked the first examples of ultrahigh resolution matrix spectroscopy in *para*-H_2.[39] These studies were followed by the work of CH_4, where rotationally resolved lines with a typical width of ~300 MHz were observed and quantitatively analyzed.[18] Since these promising results,

attempts of studying a variety of stable and unstable molecules in *para*-H_2 have been carried out. To date, molecules such as CH_3F, CH_4 have been reported.[40] In addition, atomic species such as H (D, T), N, B, O, Xe, Kr, Al, Ag, Cu, Mg, Li in *para*-H_2 have also been studied.[21,22,41]

While the chemical inertness of rare gas matrices is unrivaled, it has been shown experimentally that unstable species also have extremely long lifetime in *para*-H_2 matrix. It has been known since the late 1980s that charged species last for days in solid *para*-H_2 without observable decay. It has also been observed that hydrogen cluster ions $H(H_2)_n^+$ have lifetime of days. This may be ascribed to the cryogenic temperature at which it is difficult to acquire sufficient energy to initiate the reactions. The long lifetime allows the kinetic studies of reactions in solid hydrogen to be possible without using too sophisticated instruments. Dynamic studies of chemical reaction in *para*-H_2 matrix have also been pursued.[42]

CHAPTER III. Experimental Apparatus

The experimental apparatus designed and built from scratch for the study of infrared spectroscopy of solid H_2 is composed of a gas handling system, an inline *ortho/para* converter, and a home-made copper sample cell housed in a liquid helium cryostat which was modified from a commercial Dewar. A number of spectrometers including two commercial Fourier transform infrared spectrometers have been used for recording the spectra of samples. The details of these apparatus are discussed in this chapter.

III.1 Fourier Transformer (FT) Spectrometer

The working principle of a Fourier transform infrared spectrometer is based on the interference effect of a Michelson interferometer. As shown in the Figure III-1, a Michelson interferometer is composed of a beam splitter, a static mirror and a moving mirror. When a beam of broad band radiation enters the interferometer, it is split into two equal components by the beam splitter. Depending on the relative position of the moving and static mirrors from the beam splitter, the two components will have certain

optical path difference x. Optical interference occurs by combining these two components again. The unique power spectrum f(x) of the combined components as a function of x is known as the interferogram, which has a complicated dependence on the optical path difference due to fact that the constructive and destructive interference occur at different x depending on the frequency of light. The frequency spectrum can then be obtained by performing a Fourier transformation of the interferogram, *i.e.*,

$$F\left(\frac{1}{\lambda}\right)=\int_{-\infty}^{\infty} f(x)e^{-i\frac{2\pi x}{\lambda}}dx \qquad \text{(III.1)}$$

Figure III-1: A Schematic of a generic Michelson interferomter

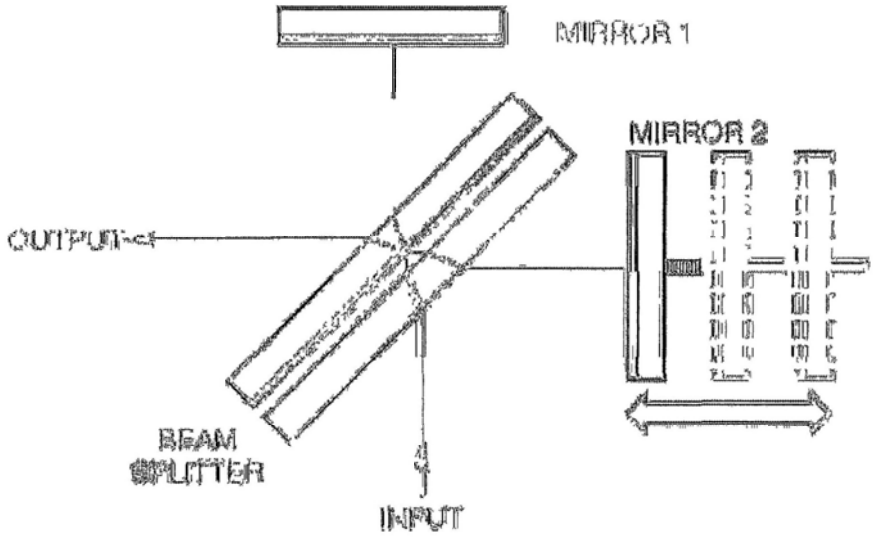

While the principle of FT spectroscopy was first introduced in 1911, commercial

FTIR spectrometers became popular and affordable only after the advancement of computer technology in the 1970s.[43] To date, the Fourier transformation can be completed in seconds using high speed computers. FTIR spectrometers have therefore become common bench top instruments replacing the conventional dispersive spectrometers to produce rovibrational spectra with improved resolution and sensitivity in much shorter time. This improvement can be realized by considering the different detection schemes in these two types of spectrometers.

In a dispersive spectrometer, the power of a small frequency interval of a broad radiation source is selected using a small slit together with a dispersion device (such as a grating or a prism) and then measured by an infrared detector. The frequency spectrum is then obtained by putting together the power spectrum of all frequency intervals. This approach has a few drawbacks. First of all, the frequency selection greatly reduced the power reaching the detector, resulting in a much lower signal to noise ratio. The improvement of signal to noise ratio requires long data acquisition time. Secondly, the spectral resolution is determined by the width of the slit. A better resolution requires a narrower slit, resulting again a reduction of power reaching the detector. Since only a small spectral region was measured each time, the complete coverage of the radiation source will require much time to complete. The required time gets longer with better resolution.

These drawbacks are addressed in Fourier transform spectroscopy. The resolution of an FTIR spectrum is determined by the maximum path difference between the two optical beams. In common practice, the resolution (σ) of an FTIR spectrometer can be estimated

by the inverse of the optical path difference x.[43] For instance, a spectral resolution of 0.1 cm^{-1} can be obtained by scanning the moving mirror for 1 cm, which can be completed in less than a second. The ultimate scanning speed of the moving mirror is restricted by the response time of the detector, and the speed of analog-to-digital data conversion. To date, spectrometers with a resolution of 0.001 cm^{-1}, corresponding to an optical path difference of about 10 m, are commercially available.

In FT spectroscopy, the total power of all frequencies emitted by the radiation source is measured by the detector simultaneously at all time. This multiplex principle results in better sensitivity, as first recognized by Fellgett,[44] due to the fact that the actual measurement time for each frequency is the same as the measurement time of the whole spectrum for FTIR spectrometers whereas in dispersive spectrometers the actual measurement time for each frequency is much less than the measurement time of the whole spectrum. The gain in signal to noise ratio (S/N) using FTIR spectroscopy is $\sqrt{N}$, where N is number of spectral segments needed to cover the entire spectrum in conventional spectrometers. In addition, the simultaneous measurement of all frequencies in FTIR spectroscopy gives rise to a much higher optical throughput (known as the Jacquinot Advantage) and thus lower noise level compared to dispersive spectrometers. The fast speed in FTIR spectroscopy makes it possible to apply signal averaging technique. Since the scanning speed of the moving mirror is determined by the response of the detector, with an appropriate detector, spectra with good S/N can be obtained by fast scanning and signal averaging (so-called coaddition) of a number of spectra in a short time. The improvement in S/N using signal averaging is $\sqrt{n}$, where n is the number of

spectra used for averaging. Since the resolution is not limited by the input aperture of the interferometer, the power level reaching the detector can be increased appreciably by choosing the appropriate aperture size. This again contributes to a better S/N in the spectra.

The fast acquisition of spectra in FTIR spectroscopy is easily realized. The multiplex principle allows the detection for the entire spectral region at all time, which significantly shortens the time of acquiring data with good S/N. As discussed above, the improvement in sensitivity requires much less time in recording a spectrum to the desired S/N. The fast scanning mechanism in obtaining the interferogram also contributes the speed accomplished by FTIR spectroscopy.

In addition, FTIR spectrometer provides much better absolute frequency calibration. By employing a frequency-stabilized He-Ne laser as an internal standard to determine accurately the optical path difference x, accurate frequency calibration can be obtained after the Fourier transformation. This characteristic is known as the Connes Advantage. It is worth to note that the resolution of the resultant frequency spectrum has little effect on the absolute frequency calibration.

In practice, there are many technical concerns in building an FTIR spectrometer. For instance, apodization is a mathematical procedure to minimize the fringes appearing at the wings of spectral transitions due to the finite optical path difference in the interferogram, the choice of the apodization function may affect the effective resolution, lineshape, and linewidth. Other considerations include phase correction, numerical filtering, analog to digital sampling, *etc.* There are a number of excellent reviews for the

detailed discussion.[43]

Two FTIR spectrometers from Bruker, namely the Vertex-70 and the IFS-120HR models, have been employed for our studies. The Bruker Vertex-70 model (Figure III-2) covers the frequency range from 400 to 25000 cm^{-1} with a unapodized resolution of 0.16 cm^{-1} using various combinations of sources, beam splitters, and detectors. In addition to usual data acquisition mode, the spectrometer is also equipped for time-resolved spectroscopy with step scan at a data acquisition rate of 200 MHz or rapid scan to obtain 60 spectra per second at resolution of 16 cm^{-1}. In covering the spectrum of solid hydrogen and impurity species, a globar or tungsten source was used with a KBr beam splitter. A HgCdTe detector was used for recording spectrum from 600 to 5000 cm^{-1} while an InSb detector was used for recording spectrum from 1800 to 10000 cm^{-1}. Since the size of our cryostat is too bulky to fit into the sample compartment, the light beam was therefore sent out from the spectrometer to our sample and then detected using external detectors. A typical spectrum was recorded at 0.2 cm^{-1} apodized resolution with 2000 coadditions. No improvement in the S/N was observed with coadditions more than 2000 times.

Figure III-2: Real photo of a Bruker Vertex-70 FTIR spectrometer

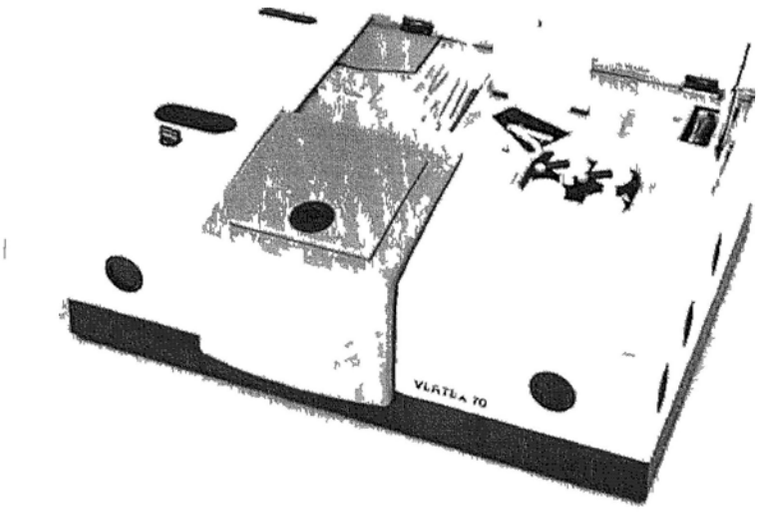

The Vertex-70 model was sufficient, in terms of spectral resolution, for studying the dynamics of nuclear spin conversion in our case However, in spectroscopic studies, transitions very often exhibited instrument-limited spectral width suggesting spectrum at higher resolution was needed for more accurate measurements For this purpose, collaboration with Professor Shuiming Hu of the University of Science and Technology of China (USTC) was established Using the Bruker IFS-120HR high resolution FTIR spectrometer (Figure III-3) and the complete experimental system for solid hydrogen matrix spectroscopy in Professor Hu's laboratory, high resolution infrared spectra of O_2 and NO were recorded The details of these experiments will be discussed in the following sessions

Figure III-3: Real photo of a Bruker IFS-120 HR FTIR spectrometer

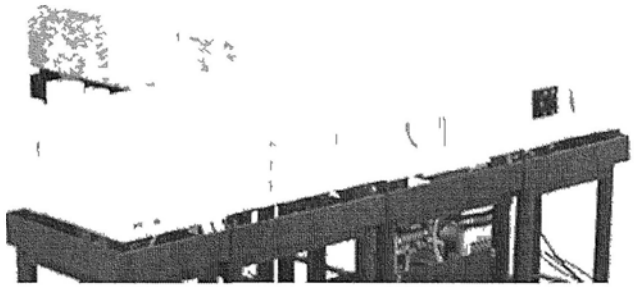

The IFS-120HR achieves a highest unapodized spectral resolution of 0.0019 cm^{-1} due to an optical path difference of about 5 m. In order to reduce the noise during the long scanning of the moving mirror, the whole spectrometer housing was evacuated. The high vacuum in the spectrometer also reduces the background absorptions of atmospheric H_2O and CO_2 molecules. This feature is particularly useful in our studies of O_2 and NO, since their transitions are located in the same region of atmospheric absorptions. Spectral at typical resolution of 0.01 to 0.005 cm^{-1} were taken using this spectrometer. Spectrum at higher resolution proved to be impractical because of the severe noise resulted. As shown in the following chapters, the improved resolution allows more features to be resolved.

III.2 Gas Handling System

The gas handling system was designed and built for a variety of experiments of solid *para*-H_2. The overall schematic of the system is shown in Figure III-4. In a typical run, normal hydrogen (n-H_2) from commercial gas cylinder was first converted to *para*-H_2 gas in an inline *ortho/para* converter A. The *para*-enriched H_2 gas from the

converter was then stored in a stainless steel vessel B. The *para*-enriched H_2 and impurity gas was then mixed at desired ratio in the stainless steel vessel C depending on the experimental requirements. The solid sample was prepared by depositing the gas/mixture gas from vessel C to the sample holder D cooled at liquid He temperature. In the following sections, each part of the gas handling system will be discussed.

Figure III-4: The schematic diagram of gas handling system.

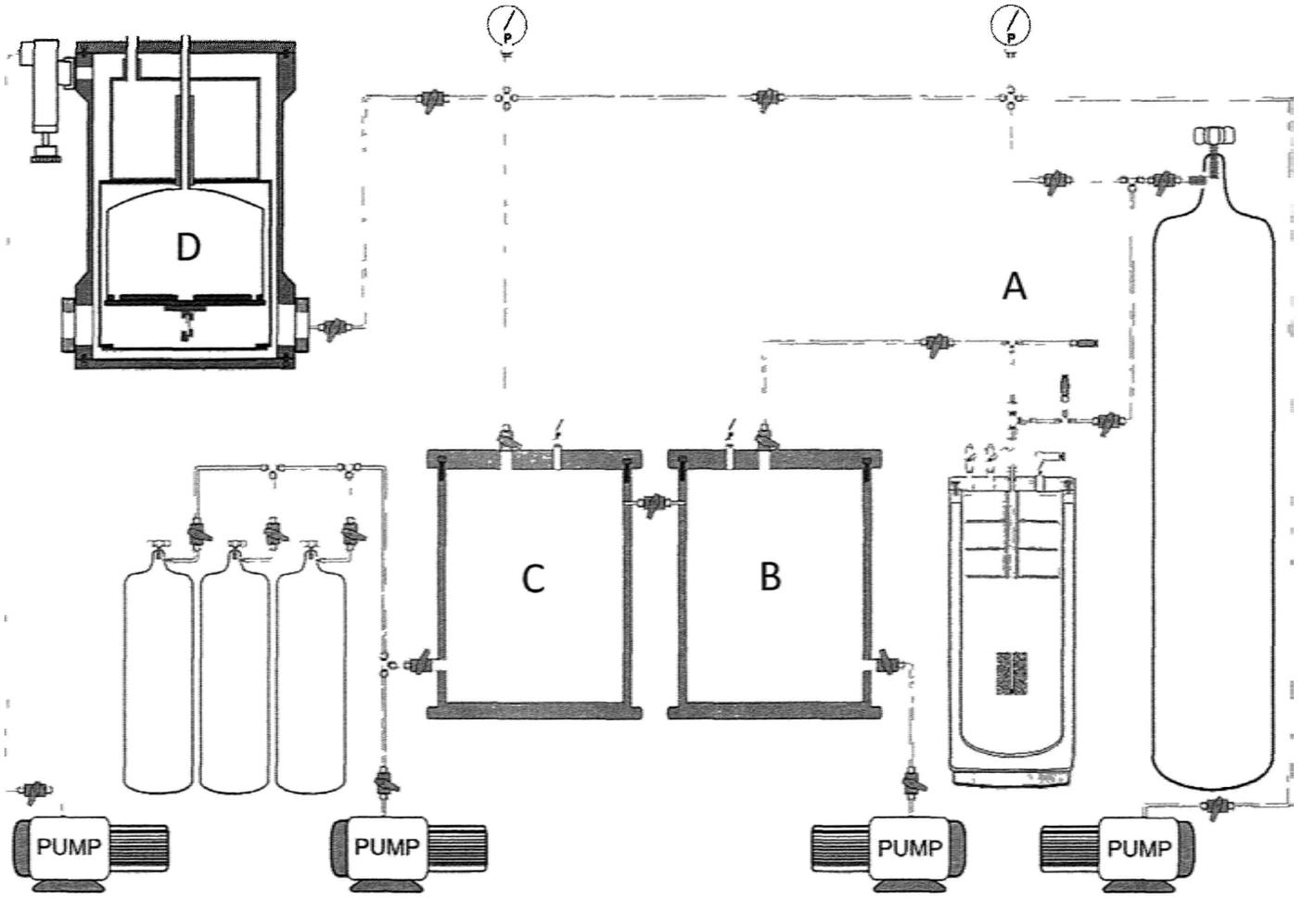

III.2.1 *Ortho/para* H_2 Converter

The use of *para*-H_2 is essential in reducing the intermolecular interactions and spectral widths of the matrix-isolated sample. As discussing in the previous chapter, the conversion from normal H_2 (with an *ortho/para* ratio of 3 to 1) to *para*-H_2 cannot be achieved by simply lowering the temperatures without the presence of an inhomogeneous magnetic field. In the temperature range of 14 to 21 K, the *ortho-para* conversion in the absence of catalysts via collision mechanism (self-conversion rate) exhibits a rate constant of 5.3×10^{-6} sec^{-1},[10] requiring weeks to obtain a mixture of ~99% *para*-H_2. Physical methods, e.g. cryogenic distillation, are inapplicable for separating *ortho* and *para* species because their physical properties are almost identical.

This *ortho/para* conversion rate can be greatly increased by using a suitable catalyst that provides an external inhomogeneous magnetic field around the absorbed hydrogen molecules so that fast equilibrium between the *ortho*-H_2 and *para*-H_2 concentrations can be achieved by lowering the temperature of the catalyst and adsorbed H_2 molecules. Based on this approach, *ortho/para* converters consisting paramagnetic ferric oxide (Fe_2O_3) from C*CHEM as the catalyst were built for the production of *para*-H_2 from normal H_2 gas.

The schematic of *ortho/para* converter is shown in Figure III-5. The Fe_2O_3 catalyst, in form of fine powder, was housed in a cylindrical stainless steel container with 5cm in diameter and 8cm in length. Two concentric stainless steel tubes of diameters 3/8 and 1/8 inch with relief valves are connected to the container as the gas inlet and outlet lines,

Figure III-5: The schematic diagram of *ortho/para* converter

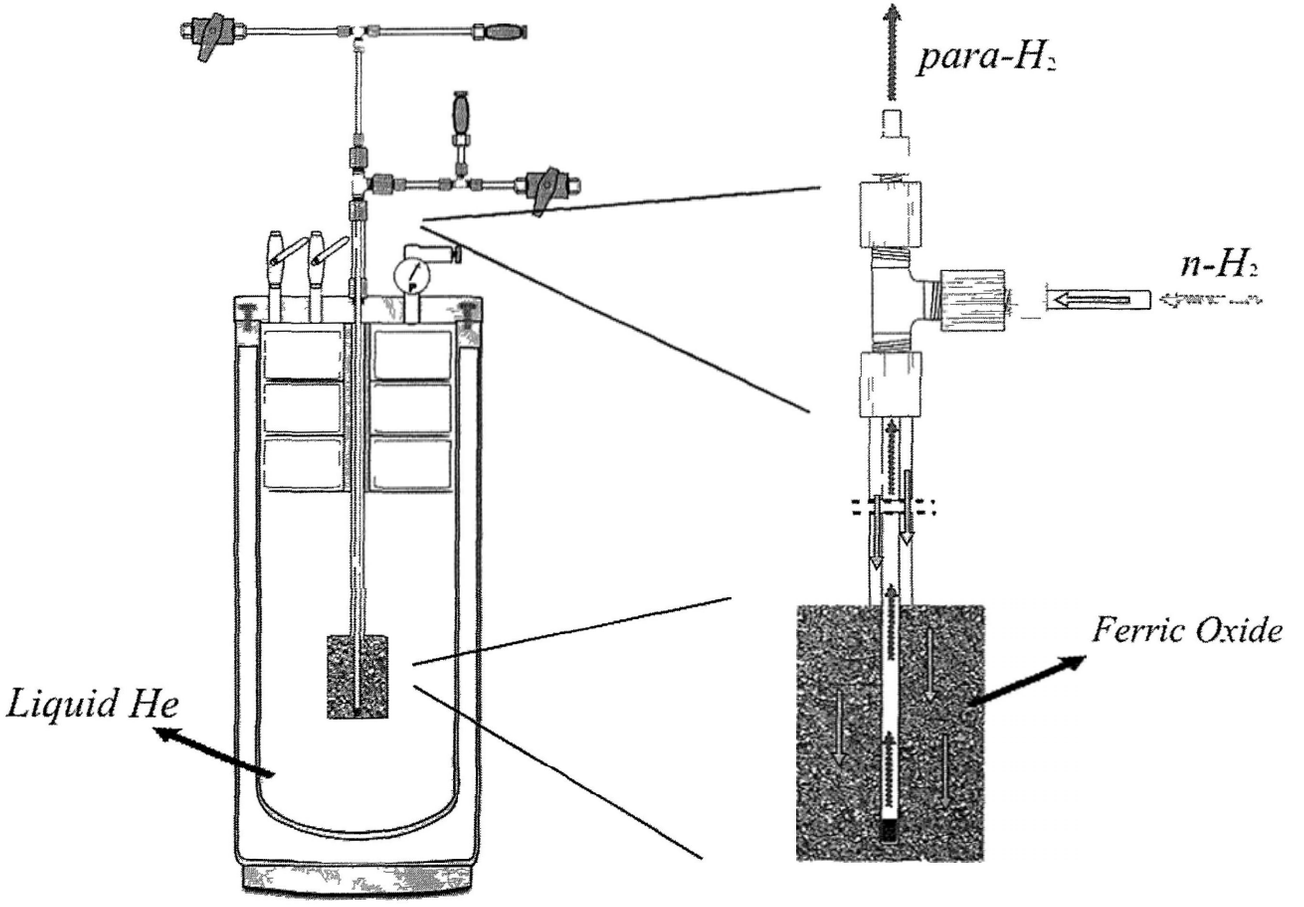

respectively. As shown in the figure, the outer tube was soldered on the top cover of the catalyst container while the inner tube fitted with gas filter at the bottom to prevent the catalyst powder from entering the vacuum system was positioned at the lower cover of the container. The temperature of catalyst container was monitored using two diode sensors (*Lakeshore Cryotronics*) installed on its top and bottom covers. The whole container system was kept in a custom-designed liquid helium Dewar (*Cryofab, Inc.*), cooled with liquid Helium. During conversion, the temperature of the converter was controlled by its distance from the liquid He level. The catalyst was initially activated by heating to a temperature range of 150 to 170 °C for a few hours while passing through hydrogen gas to remove impurity gas molecules absorbed on the surface of the catalyst. After this process, the converter was evacuated for 24 hours before used.

In the preparation of *para*-H_2 gas, the Dewar was filled with liquid Helium to about 1.5 inch high while the container was raised above the liquid He level to reach a temperature of ~14 K. Normal H_2 gas was then slowly added into the container while maintaining the temperature at 14-16 K. In order to maximize the mount of adsorbed gas, temperature fluctuation of the container was kept as small as possible. After the adsorption of H_2 gas was complete as shown by the constant temperature sensor reading, the gas input valve was closed and the container was held at about 14 K for at least one hour to let the absorbed H_2 gas to reach thermal equilibrium in the presence of an inhomogeneous magnetic field generated by the Fe_2O_3 catalyst. In order to maximize the efficiency of conversion, the conversion temperature should be just above the triple point (14 K) to allow greater mobility of H_2 molecules. Since the equilibrium *ortho*-H_2

concentration varies from around 0.004% to 0.2% in the temperature range of 14 to 20 K, it is crucial to control the temperature in this range. To release the adsorbed gas after conversion, the container temperature (catalyst temperature) was raised to about 15 K (measured vby the bottom sensor). The valve of output was opened to allow the *para*-enriched H_2 gas flow to the storage container. Special care should be taken in controlling the temperature at this stage to avoid back conversion between *para-ortho* species due to rapid increase of temperature. The typical *ortho*-H_2 content obtained following this procedure was about 0.05%.

III.2.2 Preparation of Sample Gas

The sample gas used for matrix deposition was prepared at room temperature through a pre-mixture process, which allowed the *para*-enriched H_2 and dopant gas (*e.g.* O_2 and NO) to mix thoroughly. This process was performed by using the two stainless steel vessels B and C, which were initially evacuated to $<10^{-3}$ Torr before the experiment. They were linked by a ¼ inch stainless steel tube, with a vacuum shut-off valve S to control the gas flow between them. In a typical run, the two vessels are isolated by closing the shut-off valve. Vessel B, serving as a *para*-H_2 reservoir, was filled with freshly prepared *para*-enriched H_2 gas to about 90 kPa. Depending on the experimental requirements vessel C was then filled with dopant gas to a pressure range of 0.1 to 20 Pa measured by a low-pressure membrane monometer. The gas in the vessel C was then allowed to reach a uniform distribution until the pressure reading reached a constant in a few minutes. The mixture was prepared by opening the valve S for a few seconds to

allow the high pressure *para*-enriched H_2 from vessel B to flush into the vessel C so that the desired mixing ratio was reached. This approach minimizes the possibility of back diffusion of the dopant gas into the *para*-H_2 reservoir as result of short opening time and great pressure difference between the two vessels. The mixing ratio was approximately measured by the pressure reduced in the H_2 reservoir and initial pressure of the dopant molecules in Vessel C. By comparing the final pressure of the mixture gas measured by a high pressure manometer and the initial pressure of the dopant, the accurate mixing ratio can be obtained. Using this premixing procedure, the error of the mixing ratio was estimated to be less than 0.1%, which was much smaller than other sources of experimental error that will be discussed in the following chapter.

III.2.3 Cryostat and Sample Cell

The cryostat used for the experiments on campus was a modified version of the commercial HDL-8 Dewar from Infrared Laboratories, as shown in Figure III-6. The helium Dewar is composed of two cryogenic vessels. A liquid N_2 vessel is used to directly cool a radiation shield surrounding the liquid He vessel and the cold work surface. All the interior Dewar surfaces were covered with aluminum foil in order to provide additional shielding. Along the optical axis of the Dewar, two CaF_2 windows of 1 inch in diameter were installed and sealed by o-rings to allow the passage of infrared radiation. A vacuum feedthrough on the Dewar housing was used for a stainless steel gas supply tube (1/16 inch). A $200-\mu m$ diameter nozzle modified from a syringe needle was soldered at the end of the gas line for matrix deposition.

A home-made OFHC (Oxygen Free High Conductivity) copper sample holder of 0.5 cm thickness was installed on the cold plate of the Dewar to maintain at or close to 4.2 K with liquid He filled in the can. A bore of about 1.5 cm inner diameter was cleared for the passage of light and attached with a BaF_2 windows using indium gaskets. The nozzle for mixture gas supply was placed at a distance of 1~1.5 cm in front of the BaF_2 window. This distance was found to be optimal to produce a sample of uniform thickness with reproducible optical quality as observed from the absorption spectra.

Figure III-6: Liquid helium Dewar that accommodates the sample cell

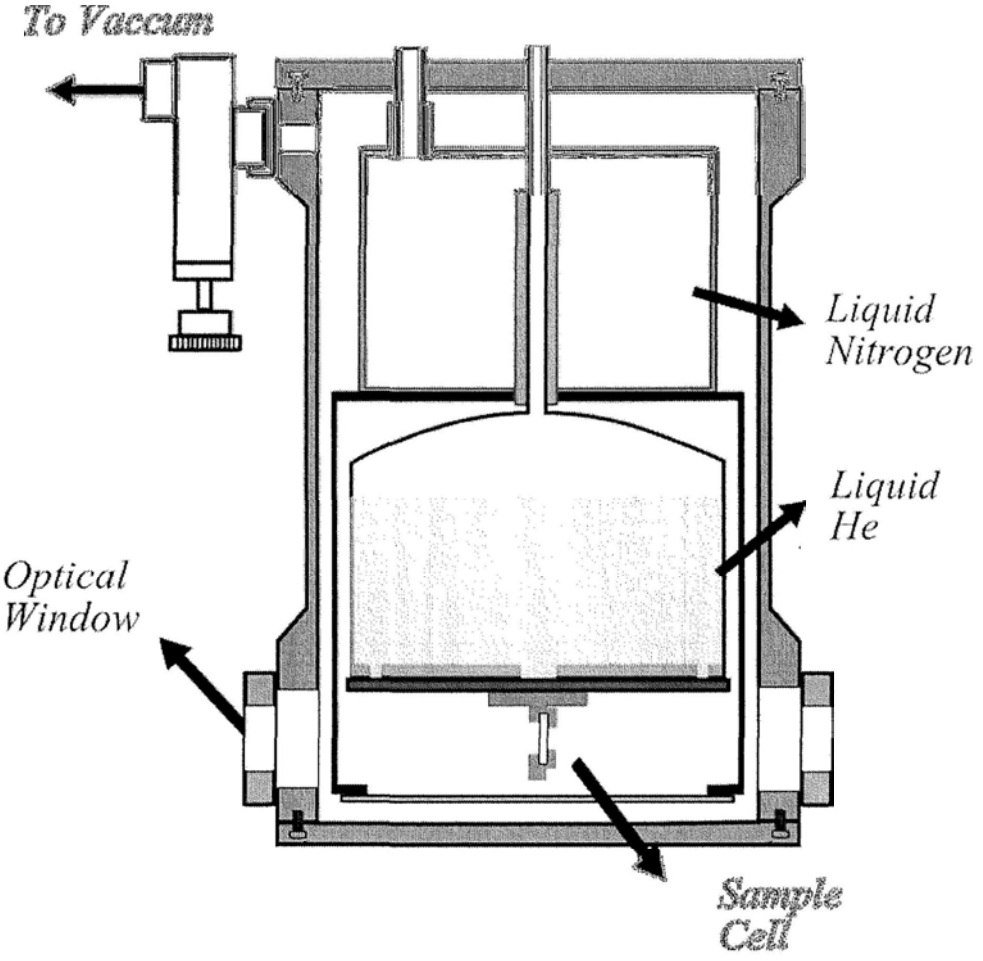

Two silicon diode temperature sensors from Lakeshore Cryotronics, (*DT670-SD*)

were used to monitor the temperatures of the cold plate and the sample cell, respectively. It was found that both sensors displayed almost identical temperature even during the deposition process suggesting excellent thermal conduction in our system. Since there was no temperature control in our Dewar, we controlled the temperature of the deposition by controlling the rate of gas flow during the deposition process.

On the other hand, the cryostat used at USTC was based on a refrigerator (*Janis SHI-4-5*) cooled by close cycle compressed helium gas. Due to the servo system of the temperature control unit, the cold finger of the cryostat always exhibits a temperature fluctuation of less than 0.05 K as measured by a silicon diode sensor from Lakeshore Cryostronics. The temperature fluctuation was expected to have little effect on the spectra. The lowest temperature achieved by the system was about 4.5 K, very close to that achieved in our liquid helium Dewar system. The sample holder was installed on the cold finger of the refrigerator. The matrix sample was prepared in a similar fashion as described above. While the two experimental setups were not identical, samples prepared in these two systems appeared to be very similar spectroscopically, as shown in the spectra taken in both cases.

III.2.4 Preparation of Matrix-isolated Species

In growing the solid sample, the mixture gas was flowing at a rate of 8×10^{-6} mol per second to deposit on the cold window of the sample cell. At this flow rate, the temperature of the substrate was about 0.1 K above the equilibrium temperature of 4.5. The low growth temperature is more desirable since the difference of melting points

between the dopant and *para*-H_2 molecules is so great that high deposition temperature tends to produce large clusters of dopant molecules, resulting in samples with low optical transparency. Dopant molecules deposited on the substrate is expected to have no further diffusion at this low temperature. Because of the excellent thermal conductivity of solid hydrogen, the optical window and the OFHC copper, the temperature was maintained steadily throughout the deposition process of about 2 hour. Samples prepared this way were optically clear suggesting little strain in the solid. This was also confirmed by the observed linewidths in the infrared spectrum.

CHAPTER IV. Catalyzed Nuclear Spin Conversion (NSC) of H_2 in the Solid State

As discussed in Chapter II nuclear spin modification behave as if they are different molecules due to the fact that they occupy different rovibrational states and the conversion between them is very slow. Nevertheless, nuclear spin conversion (NSC), while slow, has been observed for various molecules. In the case of H_2, the conversion has been studied in the gas phase as well as in the condensed phases in various experiments. In the gas phase, the conversion can occur during the collision process as a result of magnetic interactions. Since *ortho/para* H_2 occupy states with opposite parity while the magnetic interactions only connect states with the same parity, the conversion between *ortho* and *para* H_2 is strictly forbidden under the Born-Oppenheimer approximation (adiabatic approximation). However, the light nuclear mass of H_2 leads to the breakdown of the Born-Oppenheimer approximation that mixes states with opposite parity. This small mixing gives rise to the very slow *ortho-para* conversion of H_2. In the condensed phases, the conversion process can be attributed to the oscillating

gradient of the magnetic field provided by *ortho*-H_2 or paramagnetic molecules in the system. A handful of kinetic studies of both cases have been reported. The observed kinetics have been interpreted by a second-order rate law. In order to have a better understanding of the catalytic *ortho-para* conversion process, the effect of two paramagnetic species, namely O_2 and NO have been systematically studied. The results of these studies are presented in this chapter. It is hoped that these studies will lead to a better understanding on molecular diffusion and intermolecular interactions in solid hydrogen and isotopic species, a unique class of quantum crystals.

IV.1 Theoretical Background of NSC in H_2 Solids

IV.1.1 NSC of H_2 Molecules in Gas-phase and Liquid-phase

At the beginning of the last century, scientists were puzzled by two seemingly unrelated phenomena: the anomalous specific heat of hydrogen discovered by Eucken in 1912, and the line intensity alternation in molecular spectra discovered by Mecke in 1925. By discovering the existence of the two different nuclear spin modifications of hydrogen in 1929,[45] Bonhoeffer and Harteck provided the insight to uncover the solution of these two phenomena. In this experiment, the conversion rate between *ortho*-H_2 and *para*-H_2 was observed for the first time. In 1933, Wigner observed a dramatic enhancement on the NSC rate of H_2 gas in the presence of paramagnetic species, whose enhancement effect was due to the generation of an inhomogeneous magnetic field that decouples the spins of the two protons of *ortho*-H_2 molecules.[46] In

other words, the paramagnetic species serve as a catalyst for the conversion of nuclear spin modifications. Based on this idea, Winger proposed a theoretical model to account for the dependence of the observed conversion rate on the concentration of the paramagnetic substance using a collision mechanism:

$$Z_{p\to o} = \frac{8\mu_c^{\,2}\mu_p^{\,2} I\pi^2}{9h^2 r^6 k_B T} \qquad \text{(IV.1)}$$

Where $Z_{p\to o}$ is the collision efficiency that controls the catalyzed rate constant; μ_c and μ_p are, respectively, the magnetic moments of the paramagnetic species (*i.e.* catalyst) and of the proton; I is the moment of inertia of the hydrogen molecule; r is the collision distance. Winger's equation (IV.1) had been successfully applied to interpret a number of experimental observations. Farkas and Sassche found that homogeneous gas-phase conversion catalyzed by oxygen and other paramagnetic gases as well as the conversion catalyzed by paramagnetic ions in aqueous solution could be explained by the Winger's theory.[31] Harrison and MaDowell modified the Winger's theory to interpret the catalysis of the *ortho-para* conversion of hydrogen adsorbed on a paramagnetic surface at low pressures and liquid nitrogen temperatures.[47] Extensive studies had been carried out along this way, making the *ortho-para* conversion of hydrogen molecules a useful tool for surface studies as the observed catalytic rates are often related to the surface properties.

In addition to the gas-phase investigations, Wigner's model was also applied to catalytic *ortho-para* conversion of liquid hydrogen adsorbed on a paramagnetic surface. For instance, Cunningham and Johnston conducted experiments to determine the influence of the magnetic moment and concentration of paramagnetic ions adsorbed on

the surface of alumina on the conversion rate of liquid hydrogen. They found a linear dependence of conversion rate on the concentration of paramagnetic oxides.[48] The interconversion of *para*-H_2 and *ortho*-H_2 catalyzed by paramagnetic complex ions in deuterated solvents at room temperature had been reported recently by Matsumoto and Espenson.[49] An excellent linear correlation between the NSC rate constant and square of the magnetic moment of the solvated ions was found to support the collision mechanism proposed by Winger.

IV.1.2 NSC of *ortho*-H_2 in Solids: the Self-diffusion Mechanism

NSC of H_2 molecule in the solids is not so straight forward as in the cases of the gas or liquid phases since the translation motions of molecules are almost frozen out in the solids at cryogenic temperature. Since the magnetic dipolar interaction for the *ortho-para* conversion depends on r^{-6} according to Eq.(IV.1), assuming immobile molecules in the crystal lattice, one would expect a much smaller overall conversion rate in pure H_2 solids compared to the cases in gaseous or liquid phases. Furthermore, the catalytic effect of paramagnetic species on the conversion is also expected to be minimal since conversion occurs only for the *ortho*-H_2 molecules in the vicinity of the paramagnetic molecules (*e.g.* O_2) to form a sphere of *para*-H_2 surrounding the O_2 center. This sphere would poison the catalytic effect of O_2 on the NSC process as the magnetic fields from O_2 will not be experienced by *ortho*-H_2 molecules located far away.

However, as first observed by Motizuki and Nagamiya[50], the NSC rate was strongly enhanced by O_2 molecules in the solids, in contrary to the above expectation that the

ortho-para conversion of H_2 would be quenched in the solids due to the formation of *para*-H_2 layers surrounding the catalysts molecules. These observations can only be understood by assuming mobile *ortho*-H_2 molecules in solid H_2. This interesting phenomenon, however, had not drawn much attention until the direct evidence of the *ortho*-H_2 diffusion in the solids was discovered by Meyer and coworkers 1968.[51] This milestone was setup by unexpected observations of the ablation of NMR signal of isolated *ortho*-H_2 molecules, as well as the buildup of NMR signal for *ortho*-H_2 pair, after a sudden drop of temperature. These unexpected results had puzzled Meyer's group until they studied the time evolution of NMR signal at different crystal temperatures. They found that the NMR signal from the isolated *ortho*-H_2 decreased as the temperature dropped from $3K$ to $0.4K$ and reappeared to the original amplitude as the samples were re-heated to $3K$. The equilibrium was established with a time constant on the order of hours depending on temperatures and *ortho*-H_2 concentration. After being aware of the fact that the internal energy of isolated *ortho*-H_2 pairs was lower than that of the isolated *ortho*-H_2 "singles",[52] they concluded that the decrease of NMR signals was due to the dimerization of *ortho*-H_2 molecules as the sample was warmed up. This phenomenon, called as *ortho*-H_2 self-diffusion, was further confirmed and investigated through various optical experiments in other laboratories within a few years.[53-55]

Following the experimental studies, theoretical basis of *ortho*-H_2 self-diffusion in the solid hydrogen crystal based on the first principle was first investigated by Ebner and Sung's.[56] Two mechanisms, namely, quantum-mechanical tunneling and thermal

activation over a potential barrier or vacancy motion were considered in their model, where a single quantum crystal calculation was used to determine the energy levels and barrier for a molecule adjacent to a localized vacancy in hcp solid H_2. The resulting diffusion coefficient exhibited a high-temperature form $D = 6\times10^{-4} e^{-197/T}\ cm^2/s$, due to classical thermal excitation over a barrier. They also find a low-temperature term due to quantum-mechanical tunneling with activation energy of $112K$. While the high-temperature behavior was in great agreement with experiment, as mentioned above, the low-temperature behavior had yet been observed experimentally. Oyarzun and Van Kranendonk pointed out that,[57] for most experimental situations, the $J=1$ *ortho*-H_2 concentration was sufficient to reduce the quantum-mechanical tunneling by a factor of ~ 10^7 as a result of the EQQ interaction between *ortho*-H_2 molecules to give a negligible rate constant of order $10^8 - 10^{12} h^{-1}$. In other words, it is difficult to fulfill the energy conservation condition when, in an exchanging process, *ortho*-H_2 reoriented or hopped to another lattice site, because the orientation energy is large compared to the exchange energy.

Instead of "quantum-mechanical tunneling", Oyarzun and Van Kranendonk interpreted the self-diffusion effect occurred in the solids in a different manner.[58] They proposed a mechanism involving a simultaneous conversion of an *ortho*-H_2/*para*-H_2 pair into a *para*-H_2/*ortho*-H_2 pair. This simultaneous conversion was called "resonant *ortho-para* conversion" or "rotation diffusion". In a detailed calculation, a rate constant of order $2h^{-1}$, in agreement with experiments, was determined for the self-diffusion.

IV.1.3 NSC of *ortho*-H_2 in Solids Catalyzed by Paramagnetic Species

The self-diffusion of *ortho*-H_2 molecules in the solids state is responsible not only for the redistribution of *ortho*-H_2 molecules in the crystals but also for the establishment of Boltzmann distribution between $J=0$ and $J=1$ H_2 molecules due to NSC. The rate of NSC due to *ortho*-H_2 molecules is very slow, on the order of a few hours, as shown by Nagamiya in 1950s.[50] In 1990s, Shevtsov and coworkers studied the *ortho-para* conversion of solid hydrogen with small amounts of O_2 impurity in the temperature range $4.2-7K$ using NMR and observed greatly enhanced NSC rates.[59,60] They found that the conversion rate, which was substantially greater than that of the self-conversion process in pure solid H_2, showed a strong dependence on temperature and the O_2 content in the sample. By carefully checking the time evolution of the *ortho*-H_2 contents in the solids, they found that the overall rate of the catalyzed conversion in the sample was determined by the relative diffusion of *ortho*-H_2 and the O_2 impurities with a diffusion coefficient obeyed an Arrhenius behavior $D(T)=3\times10^{-11}e^{(-96/T)}cm^2/s$. This temperature dependence was interpreted in terms of vacancy-particle exchange by quantum tunneling through the intervening barrier. Few studies along this line were reported until Abouaf-Marguin and Vasserot demonstrated, using FTIR spectroscopy to study the *ortho-para* conversion rate at $4.2K$ for normal hydrogen samples double-doped with impurities H_2O/O_2, CH_3F/O_2, CH_4/O_2. While using a different monitoring technique, the observed conversion rate constants were consistent with the work by Shevtsov *et al.*

While the molecular diffusion in solid H_2 has been explained by the vacancy-particle exchange process from an intuitionistic point of view, the catalytic effect of paramagnetic impurity molecules requires preferential approaching between *ortho*-H_2 and catalyst molecules to form a pair. In the absence of intermolecular interactions, the pairing is achieved by random walk. On the other hand, intermolecular interactions will accelerate this process. It is interesting how the catalytic conversion rate is affected by intermolecular interactions.

In addressing the effect of intermolecular interactions on the NSC rate, systematic kinetic studies of NSC of solid H_2 catalyzed by O_2 and NO impurities, respectively, have been conducted. Compared to O_2 molecule, NO possesses a stronger electric dipole moment but a weaker magnetic dipole moment. A stronger electric dipole moment of NO allows faster diffusion because of stronger intermolecular electrostatic interactions, while a weaker magnetic dipole moment results a shorter conversion separation. Accurate and systematic experimental studies to investigate these two opposing effects on the NSC rate no doubt provide a test ground for quantitative theoretical computations. In the following the details of the experiments and the results will be discussed. It is hoped that these studies will shed some light on the understanding of this phenomenon and provide reliable experimental data for establishing theoretical models.

IV.1.4 Kinetic Model of Catalyzed NSC in Solid Hydrogen

In Winger's theory, the actual conversion process is considered rate determining

step and thus the time required for molecules to approach each other is not taken into account. This is true only for molecules with great mobility such as gaseous molecules. In practice, it has been shown that the assumption applies even for liquid H_2 at cryogenic temperature.[48] In solid H_2, however, the translational motion of molecules is transformed to lattice vibration, which will not efficiently facilitate the formation of molecular pairs via translation. As a result, the encounter of two originally far separated molecules in the solid may require diffusion through the lattice sites. The diffusion may also involve tunneling through periodic lattice potential due to the light mass of H_2 molecules.

In considering the diffusion to form a molecular pair, the relative diffusion coefficient $D_{rel} = D + D_c$ may be used, where D and D_c are the corresponding diffusion coefficients of the two molecules involved. In the case of *ortho*-H_2/*para*-H_2 pair, both D and D_c are the same and have to be taken into account. In the case of O_2/*ortho*-H_2 or NO/*ortho*-H_2 pair, the catalyst molecules are so much bulkier and heavier that their mobilities in the solid are much lower compared to H_2 molecules, *i.e.* $D_c << D$. It is therefore reasonable to approximate the relative diffusion coefficient by that of H_2 molecules, *i.e.* $D_{rel} \approx D$. Based on a random walk model, the diffusion coefficient of *ortho*-H_2 in the solids has been expressed as

$$D = \frac{a^2}{6\tau_d} \qquad \text{(IV.2)}$$

where a is the lattice constant and τ_d is the mean time for an *ortho*-H_2 molecule to spend in one lattice site between successive jumps (*i.e.* "jump time"). Shevtsov and coworkers have found, in their temperature-dependent NMR studies, that the diffusion

coefficient D could be fitted by an *Arrhenius-type* empirical equation

$$D(T) = (2\pm1)\times10^{-11}\exp\left[-\frac{(92\pm4)}{T}\right]cm^2s^{-1} \qquad \text{(IV.3)}$$

The diffusion-controlled catalytic NSC of *ortho*-H_2 can be understood using the following picture. An *ortho/para* conversion occurs only when the "lifetime" of *ortho*-H_2 (τ_{cc}) under the influence of catalyst is shorter than the jump time τ_d. When $\tau_{cc} \geq \tau_d$, the *ortho*-H_2 molecule would hop to another site without NSC. In other words, the catalytic effect exists only when *ortho*-H_2 molecules and the catalyst molecules are adequately close that the magnetic interactions are strong enough to give rise to fast conversion. It is convenient to define the effective conversion radius R_{eff} for the catalyst molecule so that the catalytic conversion rate constant is expressed as,[59]

$$k_{cc} = 4\pi \cdot R_{eff} \cdot D \cdot n \qquad \text{(IV.4)}$$

where $n = \sqrt{2}/a^3$ is the number density of the *hcp* lattice site. Equation(IV.4) establishes a connection between the experimentally rate constant k_{cc} with microscopic variables R_{eff} and D. It is obvious that greater magnetic interaction gives rise to a greater R_{eff}. According to Silvera and Shevtsov *et al.*, the value of R_{eff} is estimated below,

$$R_{eff} = a \cdot \left(\frac{\tau_d}{\tau_{cc}}\right)^{1/12} \qquad \text{(IV.5)}$$

by accounting for the number of nearest neighbors in hcp crystals. The catalytic lifetime τ_{cc} is estimated from the self-conversion lifetime τ_{sc} by comparing the magnitude of magnetic interactions for *ortho*-H_2/*ortho*-H_2 pair with *ortho*-H_2/X (X stands for catalyst molecule) pair. Since the interaction is proportional to the magnetic dipole moments of

the pair, we expect that

$$\frac{\tau_{sc}}{\tau_{cc}} \approx \frac{E_{cc}}{E_{sc}} \approx \left(\frac{\mu_c \mu_H}{\mu_H^{\,2}}\right)^2 \approx \left(\frac{\mu_c}{\mu_H}\right)^2 \tag{IV.6}$$

The value of τ_{sc} is related by the experimental rate constant k_{sc} of self-conversion by

$$\frac{dC}{dt} = -C\left(\frac{12C}{\tau_{sc}}\right) = -k_{sc}C^2 \tag{IV.7}$$

where C is the mole fraction of *ortho*-H_2 in the solid. The equation above assumes NSC occurs only that the catalyst and *ortho*-H_2 molecules are nearest neighbors. The factor 12 accounts for number of nearest neighbors in hcp crystals. Based on the experimental value of k_{sc} reported by Silvera,[10] τ_{sc} was estimated to be $2.4\times10^6 s$. For different catalyst molecules, we can estimate R_{eff} according to the procedure discussed above. Together with the experimental rate constant k_{cc}, we may obtain the corresponding diffusion coefficient D that provides some insights into the interactions between catalyst/*ortho*-H_2 pair.

IV.2 Kinetic Studies of NSC of Solid H_2 with O_2 and NO Dopants

IV.2.1 Experimental Details

The general experimental setup has already been described in the previous chapter. Here we will describe the detailed experimental conditions for the kinetic studies. Since the NSC kinetics is expected to be temperature-dependent, it is necessary to maintain a constant temperature throughout a time span of a few days for each experiment. This

was achieved by using a liquid helium bath under atmospheric pressure. The OFHC copper used for the cell as well as the helium container reduces the temperature gradient between the bath and the sample. Since the temperature effect on the NSC of H_2 in the solids was not the main interest of our studies, it was desirable to carry out all kinetic measurements at a constant temperature. As measured by a silicon temperature sensor installed on the sample cell, the experiments were carried out at a temperature of ~5*K*. Based on the previous studies, this temperature range gives a rate constant that is long enough for kinetic measurements with reasonable accuracy. At temperature below 4*K*, clustering of *ortho*-H_2 due to intermolecular EQQ interactions leads to non-uniform distribution of *ortho*-H_2 in the solids that may complicates the experimental conditions. In a normal run, the solid samples were deposited at a temperature of 5*K* so that samples with excellent optical quality and uniform thickness were obtained, as shown in our previous work. In order to keep the kinetic measurements consistent for both O_2 and NO impurities, the temperature was kept at $4.8 \pm 0.03K$ for a few days for collecting each set of kinetic data. As discussed below, the uncertainty in temperature is expected to give rise to an error of about 10%.

The initial *ortho*-H_2 content and concentration of paramagnetic species in the solids are of great importance in the accuracy of the kinetic studies. The initial *ortho*-H_2 content was controlled at a few percent so that *ortho*-H_2 molecules are well isolated by *para*-H_2 molecules in the solid and each set of kinetic measurements can be completed in no more than a few days. In addition, this *ortho*-H_2 content will not significantly broaden the spectral transitions, and yet provide good S/N to reduce the error in

measuring integrated intensities in the spectra for determining accurate *ortho*-H_2 content. The choice of concentrations of paramagnetic impurities, was made based on the same criteria as in the case of *ortho*-H_2, *i.e.* uniform and well-isolated distribution, proper experimental duration and sufficient S/N. After performing a series of trials, it was found that the paramagnetic impurities should be on the order of a few thousand ppm in the solids as the clustering of impurity molecules that occurs at higher concentration severely reduces the optical quality of the samples. The typical procedures of premixing the gas sample and solid H_2 crystal deposition has been described in Chapter II and therefore will not be repeated here.

IV.2.2 Observations

Figure IV-1 shows the absorption spectrum, at a spectral resolution of 0.2 cm^{-1}, of solid *para*-enriched H_2 doped with 1500 ppm O_2. The initial *ortho*-H_2 content was determined to be 4% based on the method introduced in the following section. While the optical path was purged with dry N_2 gas, the residual atmospheric water and CO_2 exhibit strong absorptions around 1600 cm^{-1} and 3750 cm^{-1}, that may mask any useful information in these regions. In order to minimize this affect, a background subtraction routine was performed so that the interference of the atmospheric absorptions could be scaled down to an acceptable level, if not completely eliminated, for studying the absorption signals due to the presence of O_2.

Figure IV-1: Mid-infrared (1400-5000 cm^{-1}) spectrum of solid *para*-enriched H_2 doped with 1500 ppm O_2.

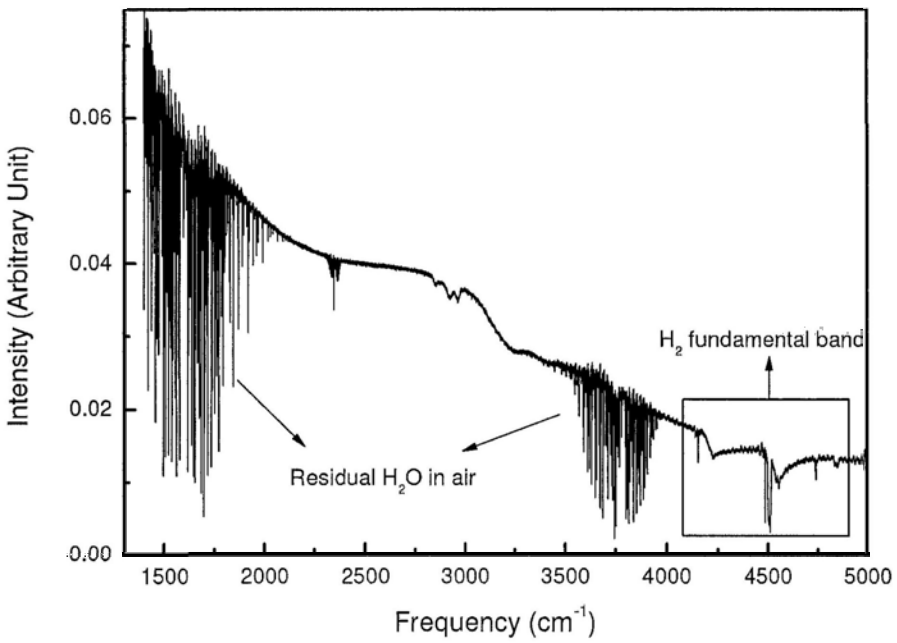

While the fundamental region (*i.e.* 4000~5000cm^{-1}) of H_2 in the solids appeared to have the usual pattern with the zero-phonon Q and S branches and the associated phonon bands (Q_R and S_R) as shown in Figure IV-2, the detailed structure of the Q branch, however, appeared to be a bit different from that of pure solid hydrogen. As shown in the inset of

Figure IV-3, the amount of *ortho*-H_2 molecules in the solids dramatically changes the appearance of the Q branch region of ~4150 cm^{-1}. In spectrum a, the Q branch was very weak in a pure solid hydrogen sample with 99.95% *para*-H_2. Spectrum b was taken from a sample of ~99.9% *para*-H_2 doped with a few ppm of CO. It is seen that the

$Q_1(1)$ transition at ~4147 cm^{-1} appears with complicated structure while the $Q_1(0)$ transition at ~4153 cm^{-1} does not show much intensity. Trace a shows the spectrum of a sample containing 4% *ortho*-H_2. The $Q_1(0)$ transition has become much more prominent because its intensity is included by *ortho*-H_2 molecules. In addition, the $Q_1(0)+S_0(1)$ & $Q_1(1)+S_0(1)$ double transitions (at 4736 cm^{-1}) associated with *ortho*-H_2 also gain much intensity. Moreover, the presence of excessive *ortho*-H_2 in the sample also significantly broadens the spectral features in the spectrum.

Figure IV-2: Raw infrared spectrum of H_2 fundamental band range of *para*-enriched H_2 solid doped with 1500 ppm O_2 taken immediately after deposition.

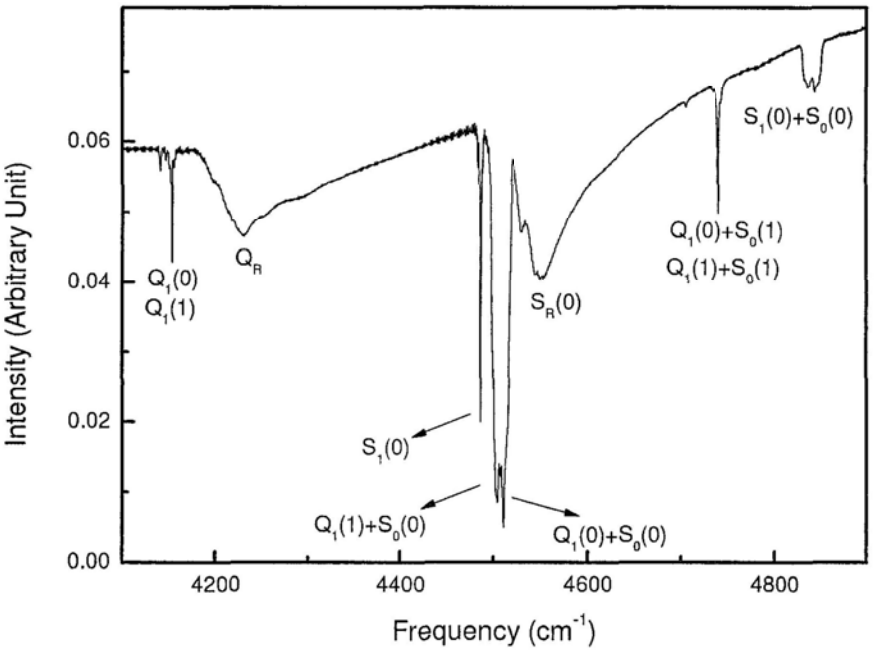

Figure IV-3: Infrared spectrum of H_2 fundamental band at 4.8 K. (a) sample contained 4% *ortho*-H_2 and 1500 ppm O_2; (b) previous pure *para*-H_2 sample of our group.

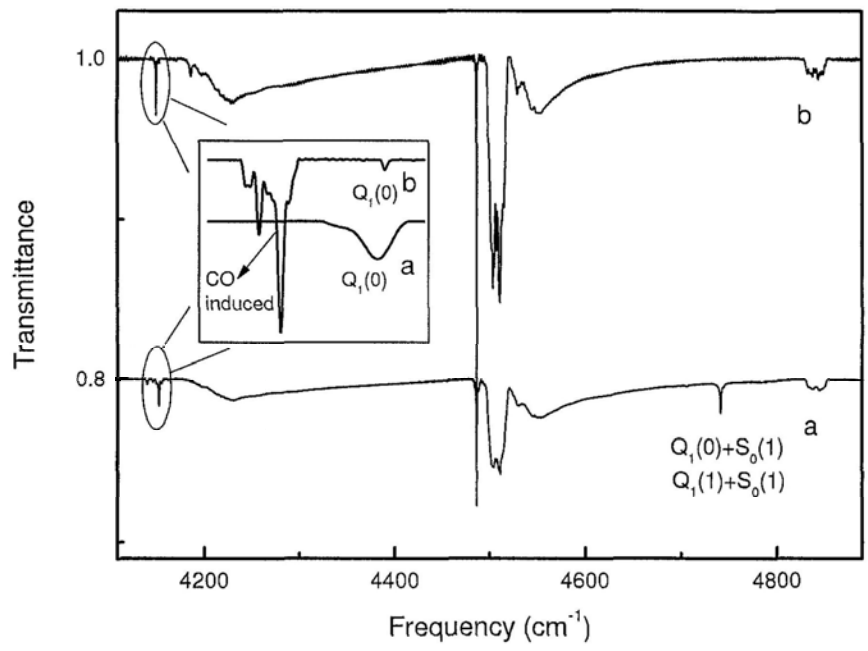

According to Boltzmann distribution, the equilibrium *ortho*-H_2 content in solid H_2 should be less than 0.01%.[39] Since the premixed gas for matrix deposition had an *ortho*-H_2 content of a few percent, the solid sample freshly prepared at ~5K will have *ortho*-H_2 in excess with respect to Boltzmann equilibrium because of the slow *ortho-para* conversion. By monitoring the time evolution of the *ortho*-H_2 content to reach thermal equilibrium in the presence of paramagnetic species, the time constant of *ortho-para* conversion can be determined. In order to monitor the temporal change of *ortho*-H_2 molecules in the solids, successive spectra of the H_2 fundamental band were recorded at different time after the sample deposition. In Figure IV-4, the $Q_1(0)+S_0(1)$ & $Q_1(1)+S_0(1)$ double transitions recorded at different time are shown. The numbers

shown in the low right of the diagram correspond to the time (in unit of minute) after the deposition when the acquisition of the spectrum starts. In the presence of 3000 ppm of O_2, the intensities of the $Q_1(0)+S_0(1)$ & $Q_1(1)+S_0(1)$ transitions drop dramatically after about 2000 minutes. Since these transitions involve simultaneous excitation of *para*-H_2/*ortho*-H_2 and *ortho*-H_2/*ortho*-H_2 pairs, respectively, the reduction of *ortho*-H_2 content will no doubt reduce their intensities. Similarly, the intensity of the Q branch transitions also drops with decreasing *ortho*-H_2 content. As pointed out by Van Kranendonk, *ortho*-H_2 molecules not only directly give rise to the $Q_1(1)$ transition at ~4147 cm^{-1} but also induce the $Q_1(0)$ transition at ~4153 cm^{-1} by a simultaneous reorientation. The temporal change of the $Q_1(0)$ transition located at 4153 cm^{-1} is shown in Figure IV-5.

Figure IV-4: Infrared absorption spectra: time evolution of $Q_1(0)+S_0(1)$ & $Q_1(1)+S_0(1)$ transition of *para*-enriched solid H_2 doped with 3000 ppm O_2.

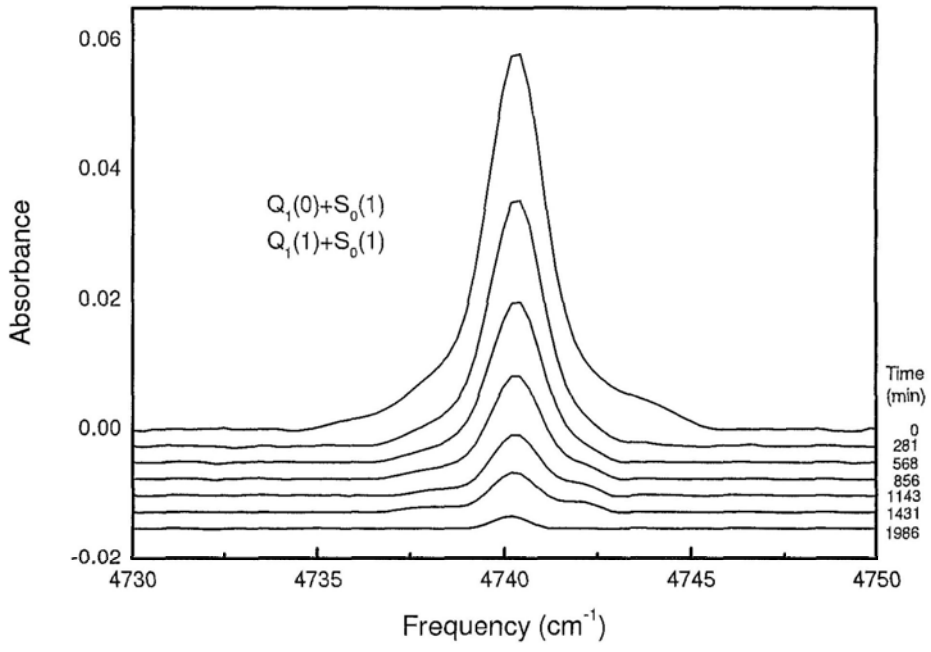

More interestingly, the inevitable trace water content in the samples also exhibited transitions due to the formation of clusters $H_2O(H_2)_n$ as shown in Figure IV-6. Because of the *ortho-para* conversion, the relative intensity of the sextet structure around 1595 cm^{-1} changes drastically. The peak at 1594 cm^{-1} became the strongest after 30 hours of *ortho-para* conversion in the presence of 3000 ppm of O_2. The detailed assignments of these transitions can be found elsewhere.[61]

Figure IV-5: Time evolution of $Q_1(0)$ and $Q_1(1)$ transition of *para*-enriched solid H_2 doped with 3000 ppm O_2.

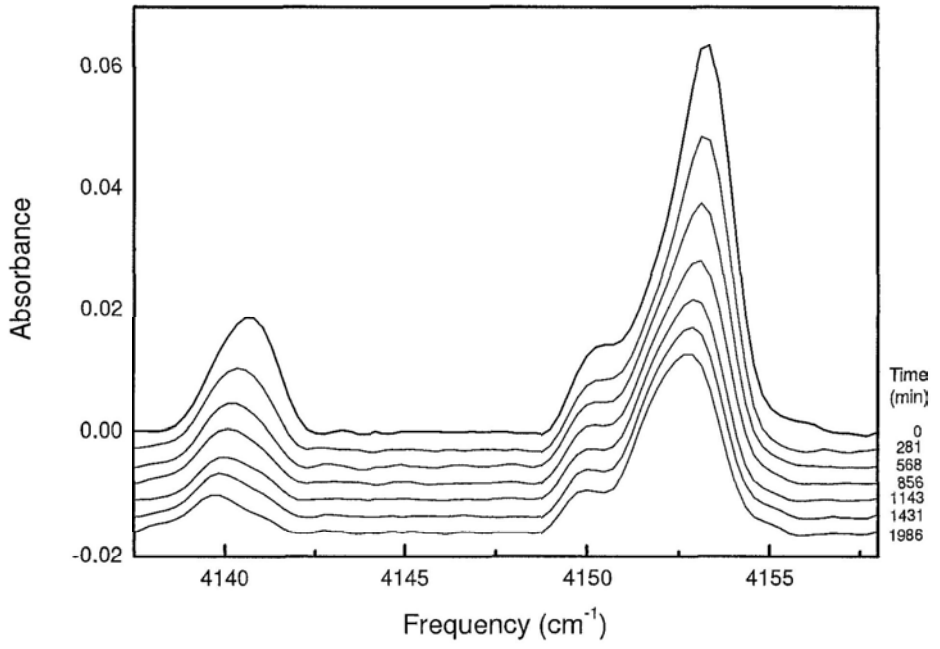

Figure IV-6: Absorption spectra of the ν_2 band of H_2O:(*ortho*-H_2)$_n$ clusters at 4.8K just after deposition and 30 hours after deposition in a sample of *para*-enriched solid H_2 doped with 3000 ppm O_2.

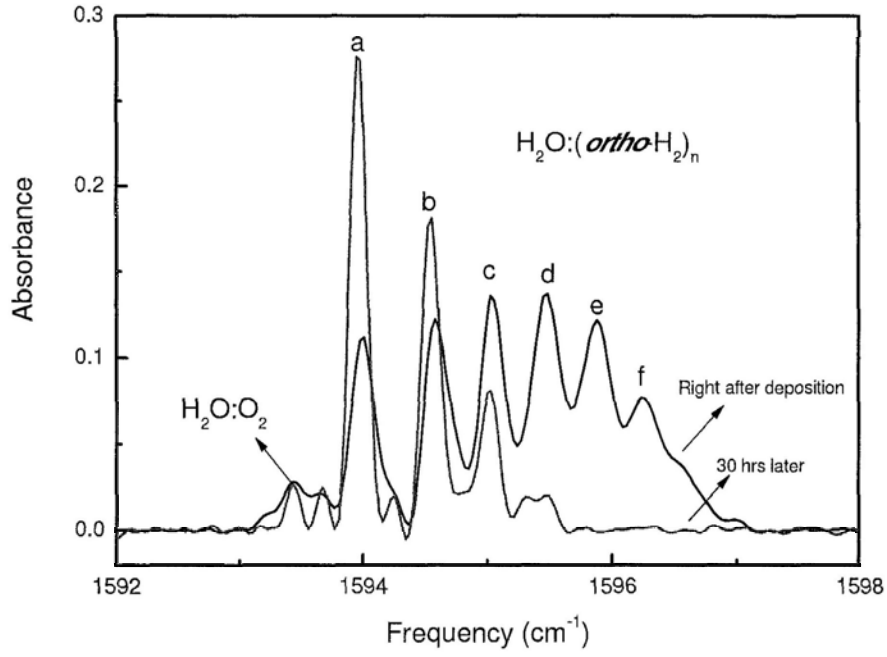

IV.2.3 Determination of the *ortho*-H_2 concentration in the solids

In order to study the kinetics of NSC in solid H_2, it is necessary to determine the *ortho*-H_2 content in solids. Several approaches, involving different experimental techniques, have been developed over the years. The commonly used methods include (a) thermodynamic methods which exploit the dependence of the free energy on the statistical distribution of *ortho*-H_2 in the lattice,[62,63] or detect the dependence of the thermal conductivity of the solids on the *ortho*-H_2 contents;[64] (b) NMR technique which monitors the characteristic spectrum intensity of the isolated *ortho*-H_2 molecules,[51] or

measure the free induction decay (FID) signals at proton frequency;[59] (c) infrared(IR) spectroscopic methods which record the transition intensities due to *ortho*-H_2 molecules in the samples. The spectroscopic approach facilitated by the high resolution and high sensitivity afforded by modern FTIR spectrometers, is capable of providing accurate measurements of *ortho*-H_2 contents with a relatively simple setup, making it an excellent choice for studies of NSC of H_2.

The determination of *ortho*-H_2 concentration in the solids using spectroscopic approach is based on the measurement of observed integrated intensities of certain *ortho*-H_2 transitions such as $S(1)$, $U(1)$ and $Q_1(1)$ lines.[65] According to the Beer-Lambert law, as shown in the following equation:

$$\tilde{\alpha} = \frac{c}{nL} \int \ln\left[\frac{I_0(\nu)}{I(\nu)}\right] d\nu / \nu \qquad \text{(IV.8)}$$

$$A(\nu) = \ln\left[\frac{I(\nu)}{I_0(\nu)}\right] \qquad \text{(IV.9)}$$

where $\tilde{\alpha}$ (in cm^3/s) is the theoretical integrated absorption coefficient; L (cm) is the length of optical path; ν (cm^{-1}) is the transition frequency; $I_0(\nu)$ and $I(\nu)$ are the initial and final light intensities respectively; $A(\nu)$ is the absorbance of the transition. Because of the short optical path of matrix samples and the weak absorption of single transitions as a result of the low concentration of *ortho*-H_2, great error is expected in measuring the corresponding integrated intensity. In order to solve this problem, Abouaf-Marguin and Vasserot have recently established an empirical law to determine the *ortho*-H_2 concentration based on the integrated intensities of double transitions.[66] Based on their model, the *ortho* and *para* concentration can be determined

using a simple empirical relationship,

$$\frac{C_o}{C_o + C_p} = \frac{1.05 \times R}{0.55 + R} \qquad \text{(IV.10)}$$

where C_o and C_p are the mole fractions of *ortho*-H_2 and *para*-H_2 respectively and R is the ratio of integrated intensities of the $Q_1(0)+S_0(1)$ & $Q_1(1)+S_0(1)$ transitions at 4736 cm^{-1} and the $Q_1(1)+S_0(0)$ & $Q_1(0)+S_0(0)$ transitions at 4505 cm^{-1}, *i.e.* $\int A(4736)d\nu \Big/ \int A(4505)d\nu$. The accuracy of the law has been supported by the excellent fitting results for their dynamics data (see Fig.3 in ref.[66]). According to Abouaf-Marguin and Vasserot, the main source of uncertainty arising from the determination of R value, as integrated intensity measurements depended on the choices of baseline and integration limits. Thus a systematic shift in the integrated intensities might exist between different personnel in performing the measurements. However, this error has no effect on the kinetic studies. By comparing the *ortho*-H_2 content of a 0.5 mm sample determined from this empirical method and the $Q_1(1)$ transition, we found that both approaches gave comparable results. This method is therefore adopted in our kinetic studies as the experimental conditions of both cases are similar.

However, as shown in Figure IV-2, the $Q_1(0)+S_0(1)$ & $Q_1(1)+S_0(1)$ transitions in our experiments appeared too strong (almost saturated), to give an accurate integrated intensity $\int A(4505)d\nu$. We thus applied another empirical relationship, found by Tam and Fajardo from their hundreds of spectra of 90 different pure and doped samples,[67]

$$\int A(4505)d\nu \Big/ \int A(4840)d\nu = 13.0 \pm 0.4 \qquad \text{(IV.11)}$$

where $\int A(4840)d\nu$ is the integrated intensity of $S_1(0)+S_0(0)$ transition of solid H_2,

whose absorbance is suitable for the accurate calculation of integrated intensity.

The *ortho*-H_2 concentration in the solid H_2 film samples of our experiments can therefore be calculated using the following equation:

$$C_o = \frac{1.05\times\int A(4736)d\nu \Big/ (13.0\times\int A(4840)d\nu)}{0.55+\int A(4736)d\nu \Big/ (13.0\times\int A(4840)d\nu)} \qquad \text{(IV.12)}$$

The kinetics of catalyzed-NSC process were therefore obtained from the time evolution of the *ortho*-H_2 concentration determined from Eq.(IV.12).

IV.2.4 Results and Discussions

By processing the successive spectra based on the procedure discussed above, the *ortho*-H_2 concentration of the solid sample at different time was determined. Figure IV-7 shows a typical decay curve of *ortho*-H_2 in a sample doped with 2500 ppm O_2. Each black dot denotes the *ortho*-H_2 concentration at the moment of starting the acquisition of the spectrum. The calculated initial *ortho*-H_2 concentration was coincided with that of the premix value, suggesting the reliability of the above mentioned method. The concentration of *ortho*-H_2 gradually approached zero as time proceeded. While the catalytic *ortho-para* conversion in a bimolecular process, the decay rate of *ortho*-H_2 is expected to follow first order kinetics, *i.e.* $C_t = C_0 e^{-t/\tau}$ since the concentration of O_2 is expected to remain unchanged. As shown in Figure IV-7, the least-squares fitting was excellent with a correlation coefficient R of 0.999, supporting the assumption of first order exponential decay. As previously stated, the depletion of *ortho*-H_2 results from two parts—self conversion process induced by the nuclear interaction between *ortho*-H_2

molecules and catalyzed conversion process induced by the magnetic moments of impurity molecules. It is therefore written as:

$$\frac{dC}{dt} = -k_{sc}C^2 - k_{cc}CC_p \qquad \text{(IV.13)}$$

where C and C_p are the concentration of *ortho*-H_2 and paramagnetic species respectively; k_{sc} is the self-conversion rate constant while k_{cc} denotes the catalyzed-conversion rate constant. According to the previous studies of Schmidt[68] and Shevtsov[59], the typical values are $k_{sc} \sim 10^{-4}\,\text{min}^{-1}$ and $k_{cc} \sim 10^{-1}\,\text{min}^{-1}$, respectively. The first term of equation (IV.13) thus could be neglected. This approximation should be applicable in our case, in which C is less than a few percentages and therefore the probability of having two *ortho*-H_2 molecules close enough to interact magnetically is very low. By neglecting self-conversion effect, (IV.13) becomes,

$$\frac{dC}{dt} = -k_{cc}CC_p \qquad \text{(IV.14)}$$

Since C_p is constant throughout the process, it can be absorbed into k_{cc} to give an observed rate constant b based on the equation above. Solving this equation gives

$$C = C_0 e^{-bt} \qquad \text{(IV.15)}$$

where C_0 is the initial *ortho*-H_2 concentration in the solids and b, the effect rate constant, is defined as,

$$b \equiv k_{cc}C_p = 1/T_1 \qquad \text{(IV.16)}$$

where T_1 is lifetime of conversion process.

Figure IV-7: The decay of *ortho*-H_2 concentration (black dots) and the fitted curve (red) shows the first order kinetics.

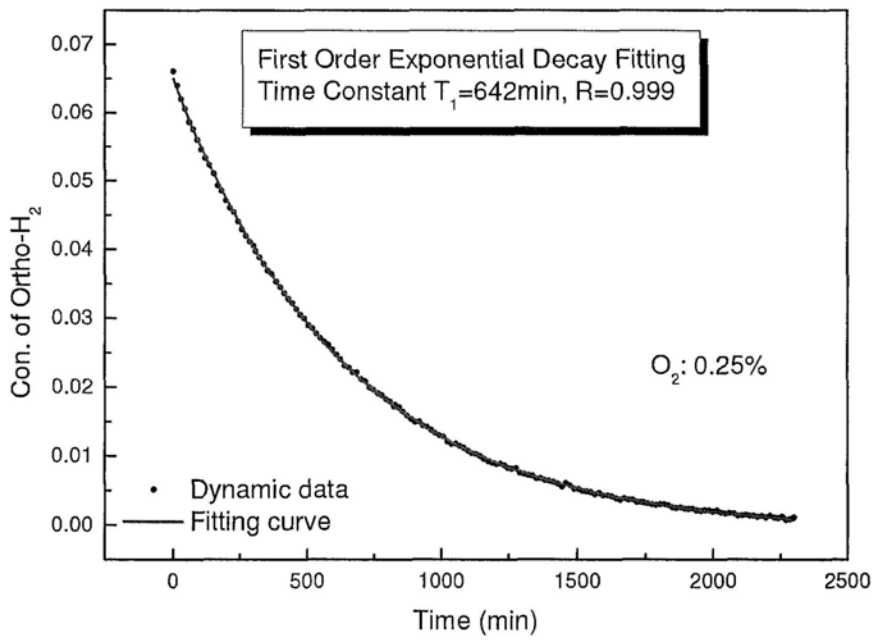

After obtaining b from the *ortho*-H_2 decay curve, k_{cc} can be determined by dividing b with C_p. By recording the decay of *ortho*-H_2 at different C_p to obtain the corresponding b values, we can determine k_{cc} by least-squares fitting from the plot of b vs. C_p. Figure IV-8 shows the plot for O_2 impurity. For each concentration of O_2, the experiments were repeated 2-3 times to ensure the consistency of data. The O_2 contents varied from 1500 ppm to 4000 ppm. In addition to the concentration listed in the figure, we also have tried samples with even lower O_2 concentration, *e.g.* 500 ppm, and even higher concentration, *e.g.* 4500 ppm. However, 500 ppm sample required much longer time for collecting the kinetic data, which introduced extra experimental error due to the long-term instrumental stability. The situations for higher O_2

concentration were even worse. Because of the low solubility of O_2 and the great difference melting point between O_2 and H_2, excessive O_2 in the solid H_2 led to serious aggregation, which jeopardized the optical quality of samples. It is seen from Figure IV-8 that in the region between 1500~3000 ppm, a linear relationship between b and C_p was obtained to give a k_{cc} of ~0.809 min^{-1}. The conversion rate constant for samples containing 4000 ppm, as shown in the figure, deviates from linearity with much higher error compared to lower concentration. We therefore, limited our investigation between 1500 ppm and 3000 ppm.

The error mainly arises from data processing, *e.g.* the choice of integration limits, the choice of the baseline, *etc.* The overall error, however, can still be estimated by comparing the results from the same data set processed by different individuals. The discrepancy between the results coming from different individuals could be treated as the total systematical error. Following that way, one of my colleagues and I have performed such test independently. The b value we obtained for a certain condition was within a few percentages and thus a maximum overall error of 10% was estimated. As shown in the figure, the discrepancies among the results from different trials on the some condition all fall in the region of error bar, suggesting reliable results with great reproducibility. We thus fitted the values of b as linear function of C_p as described above to obtain k_{cc} from the slope. In our experiments of solid H_2 doped with O_2 impurity at 4.8 K, the catalyzed rate constant k_{cc} was determined to be 0.809 min^{-1}.

Figure IV-8: Observed decay constant vs. different O_2 concentration in the solids

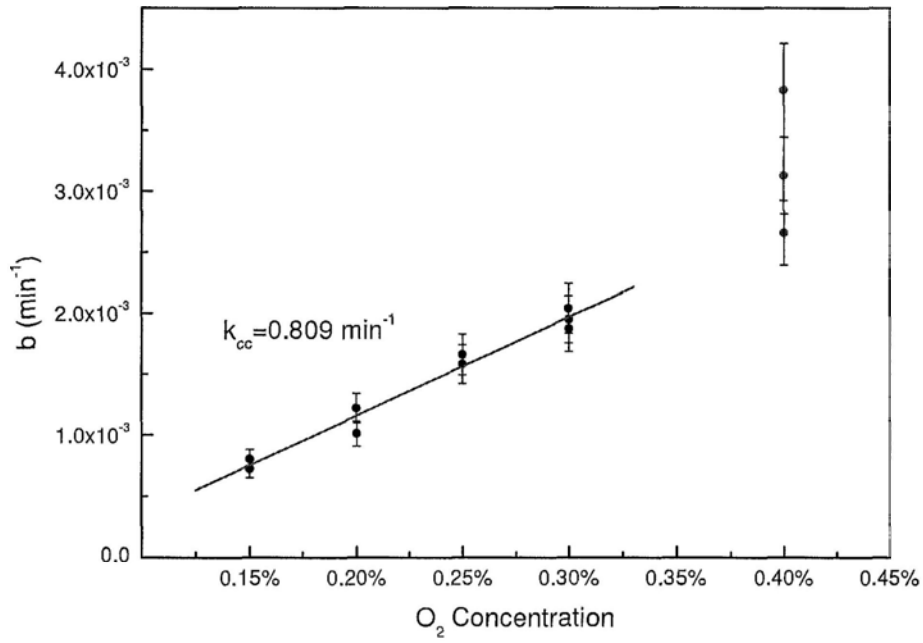

The value of the k_{cc} for O_2 from our study agrees well with that obtained by Shevtsov's group at the same temperature (fig. 6 in ref.[60]), though the experiments were carried out in totally different manners. The *ortho*-H_2 content was determined using NMR relaxation signal in Shevtsov's experiments. And within one sample period, they performed a series of NMR measurements with changing the sample temperature in order to investigate the temperature effect. Therefore, the k_{cc} they obtained at 4.8 K actually corresponded to one portion rather than the whole conversion process. On the other hand, our k_{cc} value was about five times larger than that obtained by Abouaf-Marguin, *et al.*,[69] in similar experiments at 4.2 K, compared to our studies at 4.8 K. The large discrepancy in k_{cc} may be accounted by the difference in temperature. It has been pointed out that higher temperature could speed up the H_2 diffusion in the

solids. In addition to the temperature difference, k_{cc} value was determined by Abouaf-Marguin *et al.* using no more than two sets of C_{O_2} and the relationship between k_{cc} and C_{O_2} was not clearly shown.

The linear relationship between the k_{cc} and C_{O_2} obtained in our experiments confirms the NSC process follows the second order kinetics as proposed. O_2 can be considered as immobile in the solid H_2 because of much heavier weight whereas *ortho*-H_2 can diffuse through the solids. Once the *ortho*-H_2 molecule encountered or moved close enough to an O_2 molecule, it converts to a *para*-H_2 molecule due to the magnetic interaction of O_2. The more O_2 in the solids, the higher chance that *ortho-para* conversion occurs, and therefore the greater overall catalyzed conversion rate constant.

In order to understand the driving force of the diffusion of *ortho*-H_2 in the solid, we also studied the *ortho-para* conversion of solid H_2 catalyzed by NO. Because of the electric dipole moment of NO, whose interaction with *ortho*-H_2 is expected to be stronger to give rise to a faster diffusion. On the other hand, the smaller magnetic dipole moment of NO should require closer interaction separation for the NO/*ortho*-H_2 pair. Depending on which factor dominates, it is expected that the observed NSC rate may either increase or decrease.

Using the same procedures as in the case O_2, the kinetic studies of solid H_2 doped with 0.1~0.3% of NO were carried out. For samples with NO concentration higher than 0.2%, the optical quality greatly reduced. The plot of b vs. C_p (Figure IV-9) shows that the linear fit can only be obtained with C_p no more than 0.2%. The least-squares fit gave a value of $k_{cc} = 2.185\,\mathrm{min}^{-1}$, almost 2.7 times of that for O_2. Compared to O_2,

NO is much more efficient in catalytic NSC while having a smaller magnetic dipole moment. This suggests the *ortho*-H_2 diffusion rate may be greatly accelerated towards NO.

Figure IV-9: Observed decay constant vs. different NO concentration in the solids.

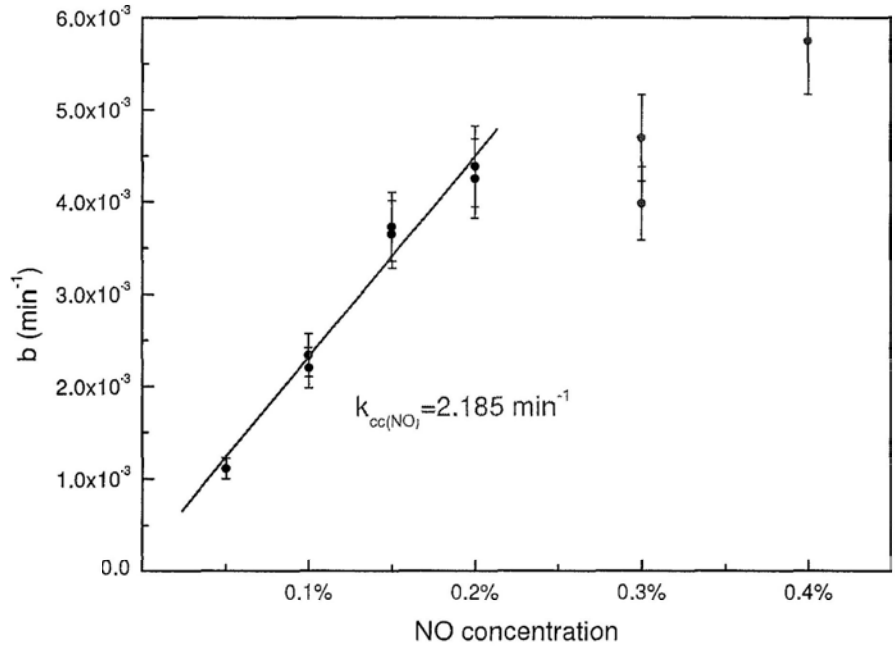

Figure IV-10: A comparison of observed rate constants of NSC catalyzed by O_2 and NO molecules.

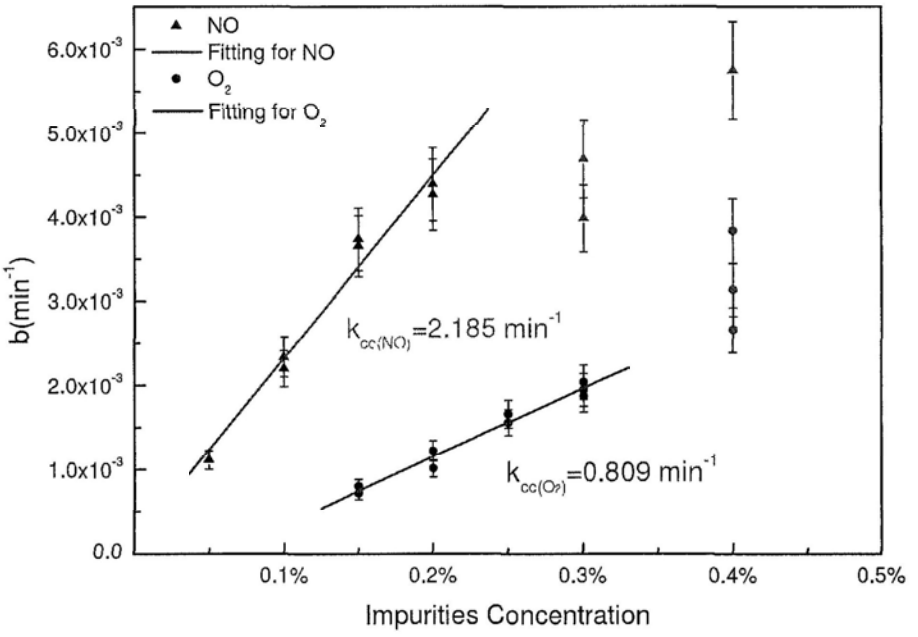

As shown in Figure IV-10, in the range from 1000 ppm to 3000 ppm of catalyst molecules, the conversion rates are linearly proportional to the concentration of catalyst in both NO and O_2 cases. However, the solid samples also appeared to have lower optical transparency at higher catalyst concentration and the catalytic efficiency dropped from the trend of linearity. This indicated the formation of aggregates of catalyst molecules at concentration greater than ~3000 ppm. Since the degree of aggregation may vary depending on the condition of matrix deposition, it is not surprised to obtain rates with greater fluctuation in this concentration range. At lower catalyst concentration, however, the linearity of the catalytic efficiency suggests that those molecules were well separated and randomly distributed in solid hydrogen matrices.

According to Winger's theory, the conversion rate constant is proportional to the square of the magnetic moments of the paramagnetic species μ^2. It therefore comes as a little surprise that NO is a more efficient catalyst for NSC since NO has a smaller magnetic dipole moment. For NO with one unpaired electron in the $^2\Pi$ electronic ground state, the spin-orbit coupling gives rise to two substates $^2\Pi_{3/2}$ and $^2\Pi_{1/2}$, corresponding to parallel and anti-parallel coupling of spin (Σ) and orbit (Λ) angular momenta, respectively. The magnetic moments of NO in these substatets are expressed as[70]

$$\mu = (\Lambda + g_s \Sigma)\mu_B \qquad \text{(IV.17)}$$

with the electron g factor $g_s \approx 2.0023$ and μ_B representing the Bohr magneton. Since the $^2\Pi_{3/2}$ state lies 123 cm^{-1} above the $^2\Pi_{1/2}$ state, it is expected that most NO molecules are in the $^2\Pi_{1/2}$ state at ~5*K*. In the $^2\Pi_{1/2}$ state with anti-parallel coupling (*i.e.* Σ and Λ have opposite sign), the net magnetic dipole is close to zero due to the cancellation of magnetic moments. On the other hand, O_2 molecules with 2 unpaired electrons in the $X^3\Sigma_g^-$ state is expected to have a magnetic dipole of about $2\mu_B$ according to Equation(IV.17). It has been shown experimentally that the molar magnetic susceptibility of NO is smaller than that of O_2 by a factor of 2.4 at room temperature. However, NO with a smaller magnetic dipole moment gives rise to a greater NSC rate constant in our experiments in which a ratio of $k_{cc}^{NO} : k_{cc}^{O_2} = 2.7:1$ has been obtained. According to Equation(IV.4), k_{cc} is related to R_{eff} and D, parameters specific to different catalyst molecules. As discussed in the kinetic model, R_{eff} is on the order of a that gives little effect on different k_{cc}. The great difference in k_{cc} for O_2 and NO is

therefore due mainly to different D values. Since the two experiments were carried out at slightly different temperatures that will give rise to different D values in both cases. From the observed difference of $T_{NO} - T_{O_2} \approx 0.03K$, a change of less than 10% in the rate constant is expected due to the change in diffusion coefficient using Equation(IV.3). In other words, the greater k_{cc} in the case of NO cannot be explained by temperature effect.

In order to ensure our observation is genuine, we deduced, in the case of O_2, the value of $D_{O_2} = 6.9\times10^{-19} cm^2 \cdot s^{-1}$ from Equation(IV.4) using $R_{eff}^{O_2} \sim 1.5a$ estimated from Equation(IV.5). This value compared favorably using the value obtained from the empirical Equation(IV.3) by Shevtsov *et al.* It should be noted that the diffusion coefficient obtained here has nothing to do with the O_2 concentration as long as it is low enough so that the random walk assumption is not violated. In the case of NO, the same approach was applied to obtain $D_{NO} = 2.1\times10^{-18} cm^2 \cdot s^{-1}$ using $R_{eff}^{NO} \sim 1.1a$ and $k_{cc} = 0.036 s^{-1}$.

The greater diffusion coefficient for NO compared to O_2 may be ascribed to the fact that there are stronger electrostatic interactions between NO/*ortho*-H_2 pair. The nonzero electric dipole moment of NO gives rise to dipole-induced dipole interaction that may cause a preferential direction for diffusion compared to the case of O_2/*ortho*-H_2 pair, in which electric quadrupole-quadrupole interaction is dominant. However, quantitative investigation of the effect of electrostatic interactions on diffusion coefficient in solid hydrogen may require Monte Carlo calculations, which is beyond the scope of our study. It is hoped that our observations will stimulate some

theoretical and computational studies on this interesting issue.

CHAPTER V. Infrared Spectra of O_2 and NO in Solid *Para*-H_2

It has been known in recent studies that solid hydrogen possesses unique properties to facilitate spectroscopic studies at unprecedented resolution. The high resolution rovibrational spectra of molecules in solid hydrogen reveal not only the motions of molecules in the solid but also details of isotropic and anisotropic intermolecular interactions in H_2 matrices. Nevertheless, the high resolution spectra observed in the H_2 matrix system are often too complex to be interpreted based on the existing theory, reflecting how little is known. In addition to studying the catalytic effect of O_2 and NO on the nuclear spin conversion of solid hydrogen, we also recorded their rovibrational spectra in solid hydrogen. It was hoped that studies of these simple diatomic molecules will shed some light on the understanding of the spectra of larger molecules.

V.1 Infrared Spectra of O_2 in Solid H_2 Matrix

As a homonuclear diatomic molecule, rovibrational transitions of O_2 are dipole forbidden. In the solid state, however, the intermolecular interactions give rise to

multipole-induced dipole that is responsible for the infrared transitions of O_2. This is the same mechanism for the infrared transitions of H_2 molecules in the solid state, as discussed in Chapter II. The infrared spectrum of O_2, while predicted to be observable, has yet to be reported, probably due to the small induced dipole moment. Following the observation of O_2-catalyzed NSC of H_2 molecules in the solid, we also attempted the search of the infrared transition of O_2 in the same system.

V.1.1 Theoretical Background

O_2 is composed of two nuclei with spin $I=0$ (Bosons). The ground electronic state of O_2 is $X^3\Sigma_g^-$ corresponding to zero projection of total electronic orbital angular momentum along the molecular axis with a spin multiplicity of 3 arising from the two unpaired electrons. The angular momentum coupling scheme in O_2 therefore follows the Hund's Case (b) in which the spin-orbit coupling is much less important than the spin-rotation coupling. The quantum number J for the total angular momentum can be obtained from rotational quantum number N and electron spin quantum number S using the triangular rule. In the case of O_2 with $S=1$, each rotational level spit into a triplet corresponding to $J=N+1$, N, and $N-1$, respectively. According to the Pauli principle, only rotational energy levels with odd N are populated for O_2 molecules while levels with even N are forbidden. The schematic diagram of rotational energy levels is depicted in Figure V-1.

Figure V-1: Schematic diagram of rotational energy splitting pattern of O_2 in gas phase. The grey dashed lines correspond to the forbidden rotational energy levels.

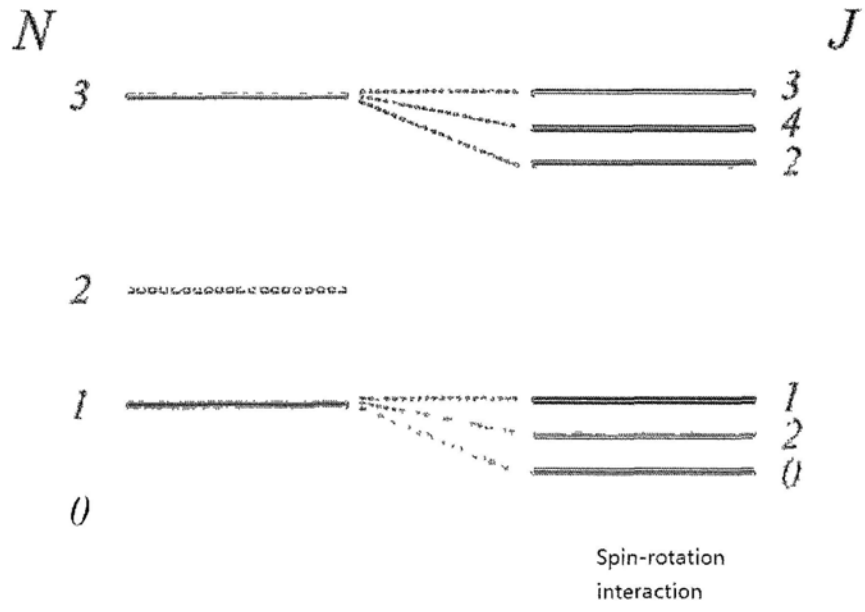

While infrared transitions of O_2 are forbidden, the rotation-vibration energy levels have been studied using Raman spectroscopy.[71] The low lying electronic transitions in the near infrared region have been extensively investigated for photodynamic therapy. Spectroscopic studies have confirmed the energy pattern in Figure V-1.

V.1.2 Observations

Based on the Raman studies of gaseous O_2, we expect its fundamental frequency should be around 1550 cm^{-1}. Because of the strong atmospheric water absorption in this region, it is difficult to observe the much weaker O_2 transitions. In order to reduce the background absorption, the optical path was purged with dry N_2 gas. Figure V-2 shows the infrared spectrum (at a spectral resolution of 0.2 cm^{-1}) of a solid H_2 sample containing

about 5000 ppm O_2 and 3.6% *ortho*-H_2 content. The dotted and solid traces correspond to the spectra taken before and after sample deposition, respectively. A weak transition at 1551.9 cm^{-1} was found, in addition to atmospheric water lines, after the deposition of solid sample. The intensity of the new feature increased gradually during the deposition process to reach a maximum value, which was still very weak, with a transmittance less than 10% after a deposition time of a few hours. Search of other transition in the region was unsuccessful. Judging from the observed frequency and linewidth of ~ 0.18 cm^{-1} (FWHM), it was assigned to the pure vibrational transition of O_2 induced by nearby *ortho*-H_2 molecules. Comparing to the gas phase value of $\nu_0 = 1556.384\,cm^{-1}$,[72,73] the observed frequency was about 4.5 cm^{-1} lower, a typical figure for molecules in solid H_2 matrix. Since the observed linewidth appeared to be instrumental limited and the seemingly asymmetric profile of the peak indicated that there might be unresolved features, studies at higher spectral resolution was necessary for a more careful investigation.

Figure V-2: Infrared spectrum of fundamental band of O_2 trapped in the solid H_2 matrix recorded at a spectral resolution of 0.2 cm^{-1}.

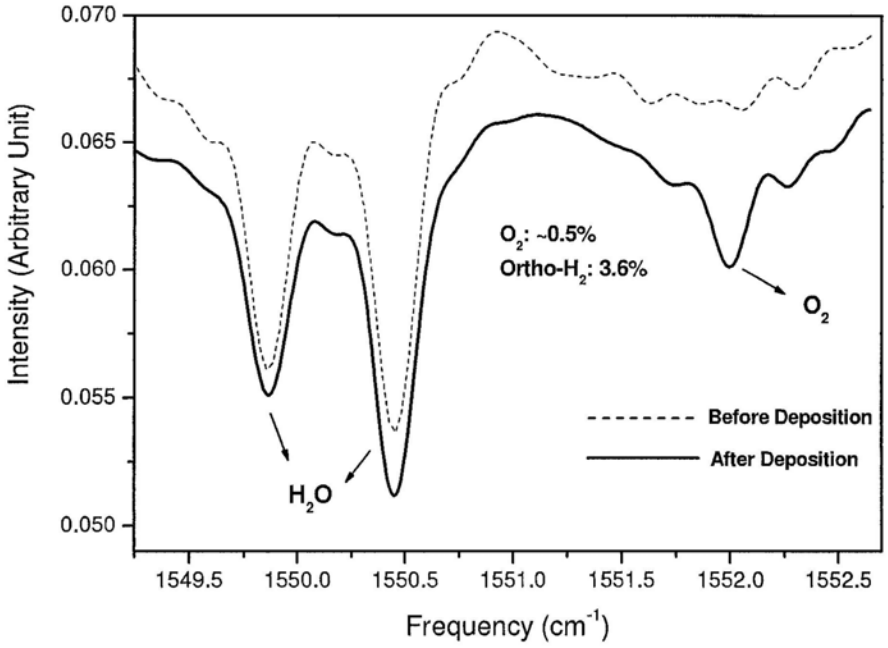

In collaborating with Professor Shuiming Hu in University of science and technology of China, we recorded the infrared spectrum at a resolution of ~0.008 cm^{-1} using a Bruker IFS-120 HR FTIR spectrometer with an ultimate resolution of 0.0013 cm^{-1}. In order to reduce the linewidth broadened by anisotropic interactions, the *ortho*-H_2 content was reduced to about ~0.05% by using two separated flows premixed in the gas line, as discussed in Chapter III. Figure V-3 shows the high resolution infrared spectrum of O_2 (3300 ppm O_2) in *para*-H_2 matrix. The clean background shown in the spectrum was ascribed to evacuating the air in the entire optical path in the spectrometer system to minimize the atmospheric absorptions. The peak shown in low resolution spectra split into a doublet with different intensity at 1551.745 cm^{-1} and 1551.787 cm^{-1}, respectively. The observed spectral linewidth was about 0.03 cm^{-1}.

It is noteworthy that recording high resolution FTIR is very time time-consuming. Since the resolution is inversely proportional to the scanning distance of the moving mirror of the spectrometer, spectra at a resolution of 0.008 cm^{-1} requires a factor of 25 more time in each scan compared to a resolution of 0.2 cm^{-1}. Moreover, the longer scanning distance also produces more noise because of the imperfection of the mirror alignment of the spectrometer and mechanical noise of mirror scanning.

The raw transmittance spectra obtained for producing Figure V-3 required a total data acquisition time of ~10 hours. However, even with such long acquisition time, the S/N ratio was still around 5. It was practically infeasible to have longer scans for better signal to noise ratio. Solids with higher O_2 concentration usually appeared a bit opaque with poor optical quality due to the aggregation of O_2 molecules. Further investigation of the transition has been limited by the low S/N of the spectrum at this stage. Attempt at studying the polarization dependence of the transition was inconclusive also because of the poor S/N.

Figure V-3: Infrared spectrum of fundamental band of O_2 in solid H_2 matrix at a spectral resolution of 0.008 cm^{-1}.

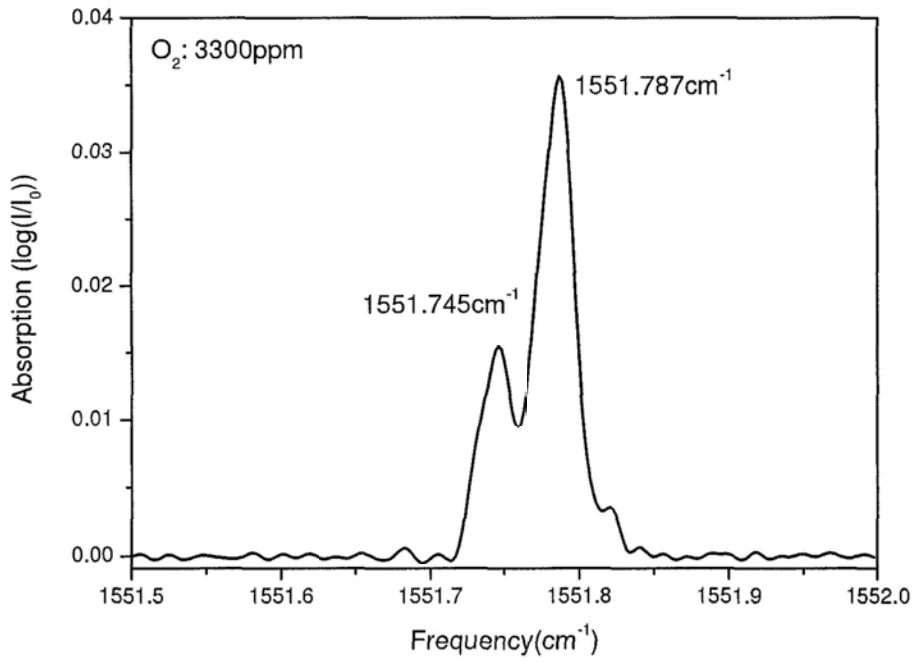

V.1.3 Preliminary Analysis and Discussion

There is little doubt that the observed transition was due to the pure vibrational transition of O_2 based on the narrow spectral width and the observed frequency. It has been known that rotational energy is dissipated to the lattice much more efficiently compared to vibrational energy. As a result, rovibrational transitions exhibit much broader linewidth as shown in the case of $S_1(1)$ and $S_1(0)$ transitions of solid para-enriched H_2. The quantitative understanding of transition frequencies and the splitting are yet to be done with just too little experimental information. While the observed linewidth was broader than the instrumental resolution of 0.008 cm^{-1}, it will

still be possible to have unresolved features if the crystal field splitting is less than the observed linewidth, as in the case of $S_1(1)$ and $S_1(0)$ of H_2 in the solid.[11] To unravel the possible unresolved features, we plan to employ the tone-burst laser spectroscopy with better resolving power to investigate this transition and its polarization dependence. These studies will provide the necessary information for the definite assignment.

Although the observations provide very limited information at this stage, the discovery of the infrared transition of O_2 molecule in the solid H_2 matrix is a great endeavor of experiment. While the results to date are preliminary, it is no doubt promising for further experimental and theoretical investigations.

V.2 Infrared Spectrum of NO in Solid H_2 Matrix

V.2.1 Theoretical Background

As an important constituent of the Earth's atmosphere, Nitric oxide together with NO_2 plays a vital role in the photochemical production of ozone in troposphere. The spectroscopic studies of NO had been known for years with experimental data well documented in the Hitran database to provide a good reference for spectroscopic constants of NO molecules.

Recent studies of NO in the condensed phase and in solid matrices, include the vibrational characterization of NO and its dimmer in the solid neon,[74] the NO related photochemistry and the diffusion of H atom in solid *para*-H_2,[75] and the hyperfine interaction between NO and He in superfluid helium droplet.[76]

NO is an open shell molecule with one unpaired electron corresponding to $^2\Pi$ electronic ground state. The strong coupling between the electron spin and orbital angular momenta (S and L) along the internuclear axis is a typical Hund's case (a) coupling scheme. The projections of S and L (Σ and Λ) combine to produce the projection of total electronic angular momentum $|\Omega| = |\Sigma + \Lambda|$ parallel to the internuclear axis. Ω and N, the rotational angular momentum, form the total angular momentum of the system J. Since $|\Sigma| = 1/2$ and $|\Lambda| = 1$, we have $\Omega = 3/2$ or $\Omega = 1/2$, respectively. Therefore the $^2\Pi$ state splits into two substates, $^2\Pi_{1/2}$ and $^2\Pi_{3/2}$, and the rovibrational energy states of NO splits into two branches accordingly.Figure V-4 shows a schematic diagram of rotational states of NO molecules. Since the $^2\Pi_{3/2}$ state lies 178 K in energy above the $^2\Pi_{1/2}$ state, it is expected that the equilibrium population of the former is insignificant at 4.5 K. As pointed by Herzberg, states with $|\Lambda| = 1$ splits into a doublet, known as Λ-type doubling, due to both the interactions between rotational motion and electronic motion. This phenomena has been observed in the gas phase, as well as in the superfluid He droplet environment.[76]

Because of the possession of permanent electric dipole moment, the rovibrational transitions of NO are infrared active. The detection of fundamental transitions was undemanding as the intensities of the features built up rapidly, in contrast to the case of O_2.

Figure V-4: The rotational levels of $^2\Pi$ state of NO in Hund's case (a). The lowest state of $^2\Pi_{3/2}$ is higher than that of $^2\Pi_{1/2}$ by 178 K in energy.

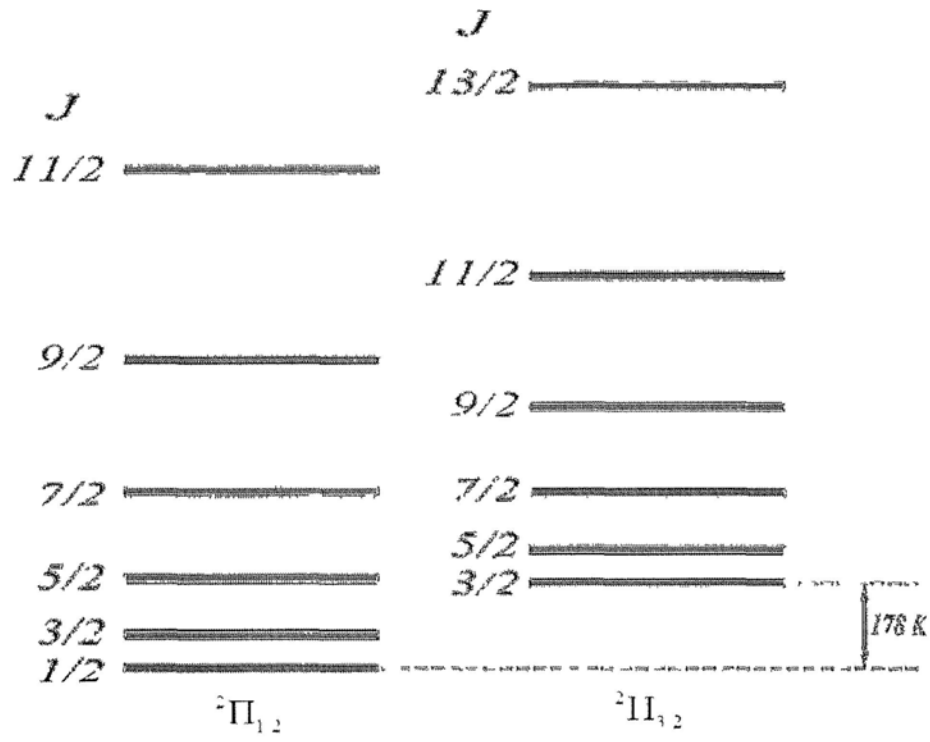

V.2.2 Observation

The experimental setup and conditions were almost identical to that used for O_2 studies, except that the NO concentration in the solid was much less than that of O_2, only on the order of a few ppm. Figure V-5 shows the typical fundamental transitions of NO embedded in solid *para*-H_2 matrix in the region of 1874 cm^{-1} at a resolution of 0.2 cm^{-1}. The NO concentration in the sample was 10 ppm and the *ortho*-H_2 content was less than 0.05%. As denoted in the spectrum, the features in the spectrum could be divided into 4 groups based on their time evolution during the sample growth. Peaks denoted by B came out first and gained the strongest intensity during the deposition. It was located at 1873.80

cm^{-1}.

Group A and Group C each has three peaks (one singlet and one doublet), whose frequency distribution were seemingly symmetric with respect to peak B. The frequency shifts of these peaks from B, as indicated in the top area of the figure, clearly illustrate this mirror image distribution. Unlike the doublet of A which is clearly resolved, the doublet of C begin to emerge with each other due to higher intensity. All three groups of peaks share reasonably sharp linewidths on the order of 0.2 cm^{-1} (FWHM).

Peak D, unlike the other features, exhibited a much broader linewidth with an atypical line shape that could not be ascribed to either Gaussian or Lorentzian functions. The attempt at finding the corresponding feature of D on the low frequency side of B was unsuccessful even with samples of greater thickness and higher NO concentration.

The overall spectrum remained unchanged at a resolution of 0.008 cm^{-1}. In addition, no observable change was found by using 100 ppm of NO. The temperature change, however, gave rise to some changes in relative intensity of the line, as shown in Figure V-6. It is clear that group C, together with peak B gained intensities at lower temperature while group A lost its intensity. This observation suggested that peaks B and C might be due to states at lowest energy.

Figure V-5: Infrared spectrum of NO trapped in solid *para*-H_2 matrix. The NO concentration used in this sample was 10 ppm, and the *ortho*-H_2 impurity was less than 0.5%.

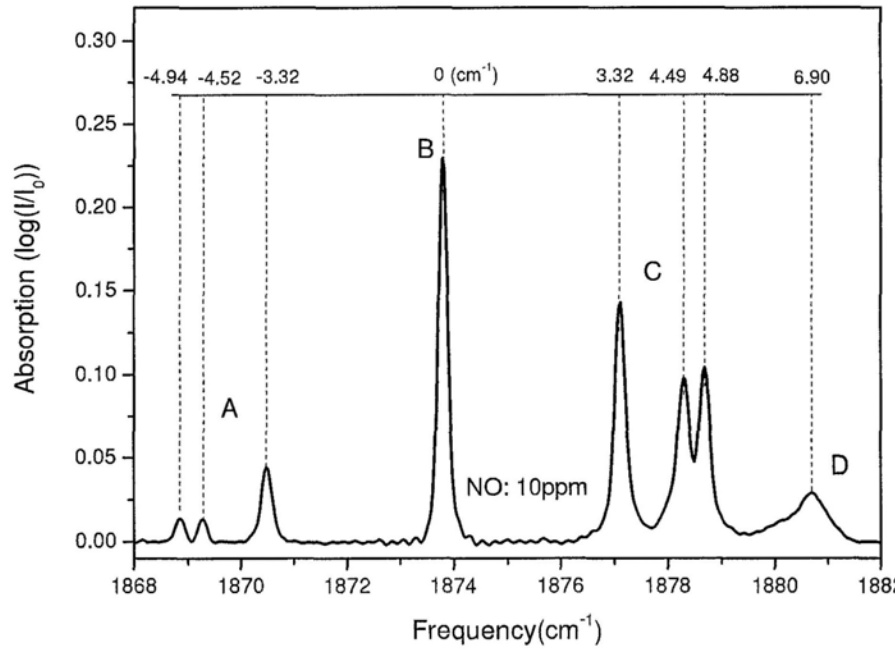

Figure V-6: Fundamental transitions of NO trapped in the solid H_2 matrix at 5 K (red trace) and 3.5 K(black trace), respectively.

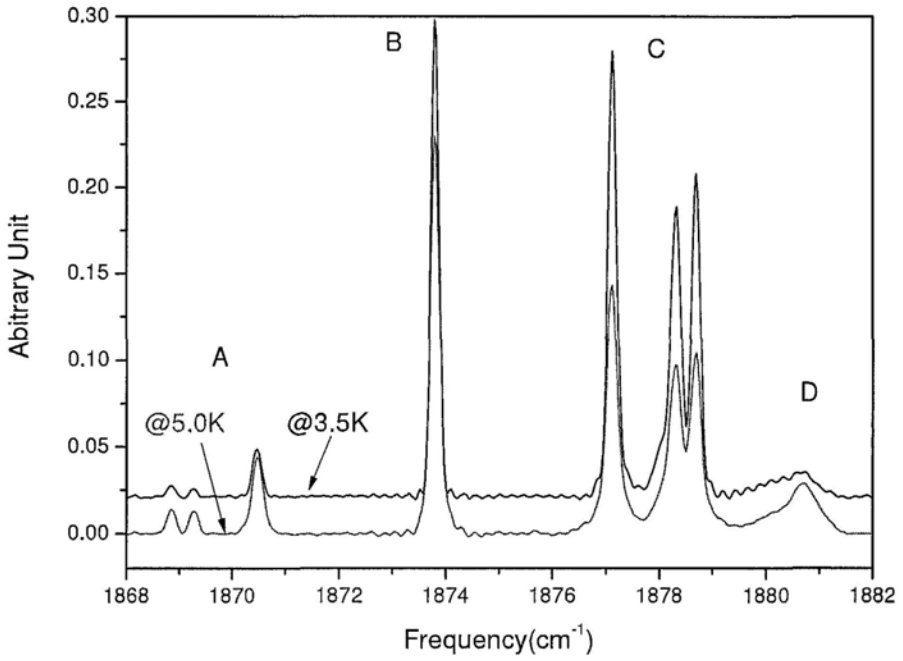

V.2.3 Preliminary Analysis and Discussion

By comparing the matrix spectrum with the corresponding gaseous spectrum (at 70 K) based on the data from Hitran database as shown in Figure V-7, we made some tentative assignments on the observed transitions. As discussed above, we expected that all the transitions were due to levels in the $^2\Pi_{1/2}$ electronic state. Judging from line width and temperature effect, transition B was assigned to the $Q(0.5)$ line, whose frequency was lowered by 2.27 cm^{-1} from the corresponding line in gas phase. As shown in Figure V-4, $J = 0.5$ is the lowest energy level, which is expected to be more populated at lower temperature to give rise to stronger transitions. Based on the same temperature effect,

group C was assigned to the $R(0.5)$ transition. The splitting may be due to different M projections in the J manifold which cannot be determined unambiguously at this stage. Group A lines reduced intensity at lower temperature, indicating that they are due to excited levels. They were therefore assigned to $P(1.5)$ transitions.

Peak D observed at the highest frequency has a distinct nature compared to other transitions. First of all, it appeared to be much broader with a spectral width of 0.8 cm^{-1}. In order to investigate whether it was related clusters of NO, we carried out experiments using different NO concentration but no observable change was found. In addition, cluster absorptions are usually lower in frequency compared to monomer absorptions, as reported in the case of neon matrix.[74] It is unlikely this peak is due to clusters of NO. The asymmetry of the line shape suggested possible unresolved structure that broadened the overall linewidth. After examining its temperature effect, we tentatively assigned it to the $R(1.5)$ line with unresolved structure. The complete tentative assignments, as listed in Table 2, are consistent with the gaseous spectrum.

Table 2: Tentative assignments for IR spectrum of NO in solid H_2 matrix

Symbols	Assignments	Frequencies (cm^{-1})
A	$P(1.5)$	1868.86
		1869.28
		1870.48
B	$Q(0.5)$	1873.80
C	$R(0.5)$	1877.12
		1878.29
		1878.68
D	$R(1.5)$	1880.70

There is little doubt that we have observed the rotational structure of the fundamental band of NO molecules in solid *para*-H_2 matrix. Based on the preliminary assignment, the band is down-shifted by 2.27 cm^{-1} from the gas phase value due to solid state perturbation. In addition, a reduced rotational constant, about 1.1 cm^{-1}, 67% of the gas phase value, was estimated from the distribution of $P(1.5)$, $Q(0.5)$, $R(0.5)$ and $R(1.5)$ transitions. Nevertheless, more experimental and theoretical studies are yet to be done in order to have definite assignment. In summary, our observations indicated that NO molecules rotate in solid *para*-H_2 matrix with little hindrance like other smaller molecules such as CO and CH_4.

Figure V-7: A comparison of gaseous spectrum (upper curve, from Hitran database) and the matrix spectrum (lower curve) of NO in the fundamental region.

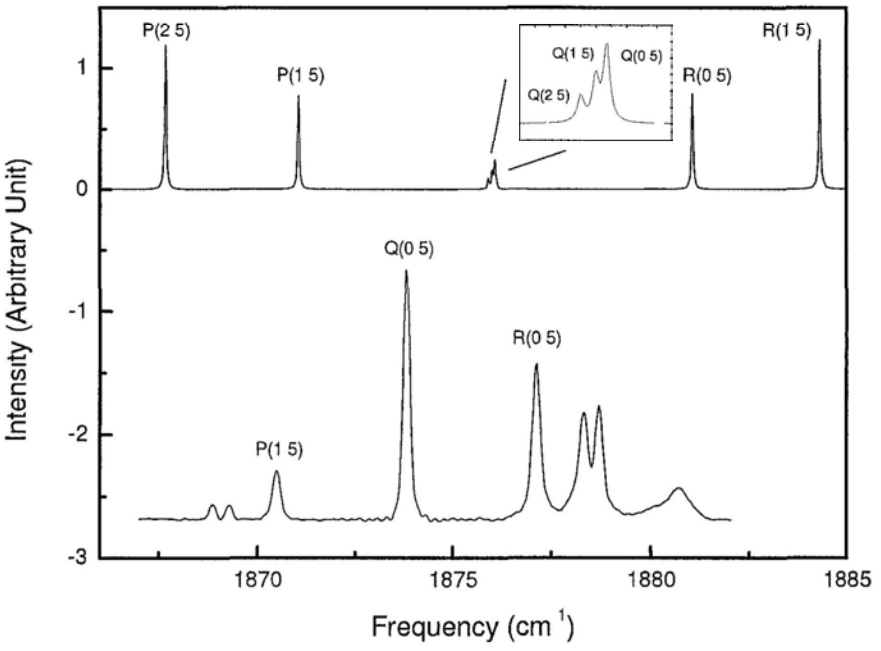

List of References

(1) Lewis, G. N.; Lipkin, D.; Magel, T. T. *J Am Chem Soc* **1941**, *63*, 3005.

(2) Whittle, E.; Dows, D. A.; Pimentel, G. C. *J Chem Phys* **1954**, *22*, 1943.

(3) Meyer, C. *Low temperature spectroscopy; optical properties of molecules in matrices, mixed crystals, and frozen solutions*; American Elsevier Pub. Co.: New York,, 1971.

(4) Lin, C. Y.; Krantz, A. *Journal of the Chemical Society-Chemical Communications* **1972**, 1111.

(5) Chapman, O. L.; Mcintosh, C. L.; Pacansky, J. *J Am Chem Soc* **1973**, *95*, 244.

(6) Pong, R. G. S.; Shirk, J. S. *J Am Chem Soc* **1973**, *95*, 248.

(7) Dunkin, I. R. *Chem Soc Rev* **1980**, *9*, 1.

(8) Dunkin, I. R. *Matrix-isolation techniques : a practical approach*; Oxford University Press: Oxford ; New York, 1998.

(9) Dubost, H. *Chem Phys* **1976**, *12*, 139.

(10) Silvera, I. F. *Rev Mod Phys* **1980**, *52*, 393.

(11) Van Kranendonk, J. *Solid hydrogen : theory of the properties of solid H b2 s, HD, and D b2 s*; Plenum Press: New York, 1983.

(12) Okumura, M.; Chan, M.-C.; Oka, T. *Phys Rev Lett* **1989**, *62*, 32.

(13) Chan, M.-C.; Lee, S. S.; Okumura, M.; Oka, T. *J Chem Phys* **1991**, *95*, 88.

(14) Chan, M.-C.; Okumura, M.; Gabrys, C. M.; Xu, L.-W.; Rehfuss, B. D.; Oka, T. *Phys Rev Lett* **1991**, *66*, 2060.

(15) Chan, M.-C.; Xu, L.-W.; Gabrys, C. M.; Oka, T. *J Chem Phys* **1991**, *95*, 9404.

(16) Momose, T.; Weliky, D. P.; Oka, T. *J Mol Spectrosc* **1992**, *153*, 760.

(17) Oka, T. *Annu Rev Phys Chem* **1993**, *44*, 299.

(18) Momose, T.; Miki, M.; Wakabayashi, T.; Shida, T.; Chan, M. C.; Lee, S. S.; Oka, T. *J Chem Phys* **1997**, *107*, 7707.

(19) Momose, T.; Shida, T. *B Chem Soc Jpn* **1998**, *71*, 1.

(20) Chan, M. C.; Okumura, M.; Oka, T. *J Phys Chem A* **2000**, *104*, 3775.

(21) Anderson, D. T.; Hinde, R. J.; Tam, S.; Fajardo, M. E. *J Chem Phys* **2002**, *116*, 594.

(22) Hoshina, H.; Kato, Y.; Morisawa, Y.; Wakabayashi, T.; Momose, T. *Chem Phys* **2004**, *300*, 69.

(23) Momose, T.; Oka, T. *J Low Temp Phys* **2005**, *139*, 515.

(24) Lee, Y. P.; Wu, Y. O.; Lees, R. M.; Xu, L. H.; Hougen, J. T. *Science* **2006**, *311*, 365.

(25) Chan, M.-C.; Song, Y.; Yan, L. *Chem Phys Lett* **2009**, *468*, 166.

(26) Shui-Ming, H.; Gang, X.; Shan-Xi, T.; Lei, W.; Jun-He, D.; Wen-Ping, D.; Lei, W.; Yang, C. *Vib Spectrosc* **2009**, *50*, 36.

(27) Cox, K. D.; Williamson, K. D. *Hydrogen, its technology & implications*; CRC Press: Cleveland, 1977.

(28) Souers, P. C. *Hydrogen properties for fusion energy*; University of California Press: Berkeley, 1986.

(29) Levine, I. N. *Quantum chemistry*; 5th ed.; Prentice Hall: Upper Saddle River, N.J., 2000.

(30) Herzberg, G. *The spectra and structures of simple free radicals; an introduction to molecular spectroscopy*; Cornell University Press: Ithaca,, 1971.

(31) Farkas, A. *Orthohydrogen, parahydrogen and heavy hydrogen*; The University press: Cambridge Eng., 1935.

(32) Fenner, W. R.; Hyatt, H. A.; Kellam, J. M.; Porto, S. P. S. *Journal of the Optical Society of America* **1973**, *63*, 73.

(33) Nosanow, L. H. *Physical Review* **1966**, *146*, 120.

(34) Klein, M. L.; Venables, J. A. *Rare gas solids*; Academic Press: London ; New York, 1976.

(35) Pauling, L. *Physical Review* **1930**, *36*, 430.

(36) Cradock, S.; Hinchcliffe, A. J. *Matrix isolation : a technique for the study of reactive inorganic species*; Cambridge University Press: Cambridge ; New York, 1975.

(37) Abe, H.; Yamada, K. M. T. *Struct Chem* **2003**, *14*, 211.

(38) Brus, L. E.; Bondybey, V. E. *J Chem Phys* **1976**, *65*, 71.

(39) Chan, M.-C. Ph.d dissertation, The University of Chicago, 1991.

(40) Yoshioka, K.; Anderson, D. T. *J Chem Phys* **2003**, *119*, 4731.

(41) Andrews, L.; Xuefeng, W. *Rev Sci Instrum* **2004**, *75*, 3039.

(42) Momose, T.; Fushitani; sect; Mizuho; Hoshina; para; Hiromichi *Int Rev Phys Chem* **2005**, *24*, 533.

(43) Griffiths, P. R.; Haseth, J. A. d. *Fourier transform infrared spectrometry*; J. Wiley: New York etc., 1986.

(44) Fellgett, P. *Journal De Physique* **1967**, *28*, 165.

(45) Bonhoeffer, K. F.; Harteck, P. *Naturwissenschaften* **1929**, *17*, 182.

(46) Wigner, E. *Z physik Chem* **1933**, *B23*, 28.

(47) Harrison, L. G.; McDowell, C. A. *Proceedings of the Royal Society of London. Series A. Mathematical and Physical Sciences* **1953**, *220*, 77.

(48) Cunningham, C. M.; Johnston, H. L. *J Am Chem Soc* **1958**, *80*, 2377.

(49) Matsumoto, M.; Espenson, J. H. *J Am Chem Soc* **2005**, *127*, 11447.

(50) Motizuki, K.; Nagamiya, T. *J Phys Soc Jpn* **1956**, *11*, 654.

(51) Amstutz, L. I.; Thompson, J. R.; Meyer, H. *Phys Rev Lett* **1968**, *21*, 1175.

(52) Harris, A. B.; Amstutz, L. I.; Meyer, H.; Myers, S. M. *Physical Review* **1968**, *175*, 603.

(53) Boggs, S. A.; Welsh, H. L. *Can J Phys* **1973**, *51*, 1910.

(54) Roffey, B. J.; Boggs, S. A.; Welsh, H. L. *Can J Phys* **1974**, *52*, 2451.

(55) Hardy, W. N.; Berlinsky, A. J.; Harris, A. B. *Can J Phys* **1977**, *55*, 1150.

(56) Ebner, C.; Sung, C. C. *Phys Rev A* **1972**, *5*, 2625.

(57) Oyarzun, R.; Van Kranendonk, J. *Phys Rev Lett* **1971**, *26*, 646.

(58) Oyarzun, R.; Vankrane.J *Can J Phys* **1972**, *50*, 1494.

(59) Shevtsov, V.; Scherbakov, A.; Malmi, P.; Ylinen, E.; Punkkinen, M. *J Low Temp Phys* **1996**, *104*, 211.

(60) Shevtsov, V.; Ylinen, E.; Malmi, P.; Punkkinen, M. *Phys Rev B* **2000**, *62*, 12386.

(61) Abouaf-Marguin, L.; Vasserot, A. M.; Pardanaud, C.; Stienlet, J.; Michaut, X. *Chem Phys Lett* **2008**, *454*, 61.

(62) Ramm, D.; Meyer, H. *J Low Temp Phys* **1980**, *40*, 173.

(63) Minchina, I. Y.; Bagatskii, M. I.; Manzhelii, V. G.; Krivchikov, A. I. *Fizika Nizkikh Temperatur* **1984**, *10*, 1051.

(64) Calkins, M.; Meyer, H. *J Low Temp Phys* **1984**, *57*, 265.

(65) Mishra, A. P.; D'Souza, R.; Balasubramanian, T. K. *J Mol Spectrosc* **2006**, *235*, 206.

(66) Abouaf-Marguin, L.; Vasserot, A. M. *Chem Phys Lett* **2008**, *460*, 82.

(67) Tam, S.; Fajardo, M. E. *Appl Spectrosc* **2001**, *55*, 1634.

(68) Schmidt, F. *Phys Rev B* **1974**, *10*, 4480.

(69) Abouaf-Marguin, L.; Vasserot, A. M.; Lekic, A. *Chem Phys Lett* **2009**, *470*, 228.

(70) Archibald, G.; Brief, E.; Lei, C.; Pausak, T.; Hayden, M. E. *Phys. Rev. A* **2006**, *73*, 8.

(71) Loete, M.; Berger, H. *J Mol Spectrosc* **1977**, *68*, 317.

(72) Butcher, R. J.; Willetts, D. V.; Jones, W. J. *Proceedings of the Royal Society of London Series a-Mathematical and Physical Sciences* **1971**, *324*, 231.

(73) Loete, M.; Berger, H. *J Mol Spectrosc* **1977**, *68*, 317.

(74) Kometer, R.; Legay, F.; Legay-Sommaire, N.; Schwentner, N. *The Journal of Chemical Physics* **1994**, *100*, 8737.

(75) Fushitani, M.; Momose, T. *Low Temp Phys+* **2003**, *29*, 740.

(76) von Haeften, K.; Metzelthin, A.; Rudolph, S.; Staemmler, V.; Havenith, M. *Physical Review Letters* **2005**, *95*, 215301.